Efficient and low-noise single-photon-level frequency conversion interfaces using silicon nanophotonics

Qing Li,[1,2,*] Marcelo Davanço,[1] and Kartik Srinivasan[1,†]

[1]*Center for Nanoscale Science and Technology, National Institute of Standards and Technology, Gaithersburg, MD 20899, USA*

[2]*Maryland NanoCenter, University of Maryland, College Park, MD 20742, USA*

(Dated: February 24, 2016)

Abstract

Optical frequency conversion has applications ranging from tunable light sources to telecommunications-band interfaces for quantum information science. Here, we demonstrate efficient, low-noise frequency conversion on a nanophotonic chip through four-wave-mixing Bragg scattering in compact (footprint $< 0.5 \times 10^{-4}$ cm^2) Si_3N_4 microring resonators. We investigate three frequency conversion configurations: (1) spectral translation over a few nanometers within the 980 nm band, (2) upconversion from 1550 nm to 980 nm, and (3) downconversion from 980 nm to 1550 nm. With conversion efficiencies ranging from 25 % for the first process to > 60 % for the last two processes, a signal conversion bandwidth > 1 GHz, < 60 mW of continuous-wave pump power needed, and background noise levels between a few fW and a few pW, these devices are suitable for quantum frequency conversion of single photon states from InAs quantum dots. Simulations based on coupled mode equations and the Lugiato-Lefever equation are used to model device performance, and show quantitative agreement with measurements.

Introduction

Efficient and low-noise frequency conversion has many applications in classical and quantum photonics, for example, casting signals to specific spectral channels for wavelength multiplexing, accessing spectral regions for which high-performance detectors are available, and connecting visible quantum memories with the low-loss telecommunications band. Years of progress in developing frequency conversion technology in both $\chi^{(2)}$ and $\chi^{(3)}$ nonlinear media[1,2], typically based on centimeter long crystals[3] and meter long optical fibres[4], has enabled researchers to demonstrate frequency conversion of quantum states, or quantum frequency conversion (QFC)[5], down to the level of single photon Fock states[6].

Nanophotonic geometries are an attractive way to miniaturize, scale, and customize optical components compared to conventional technology. In particular, microresonators with high quality factor (Q) and small mode volume offer small power budget and device size. Nonlinear wave mixing in the silicon platform (including silicon nitride and silicon dioxide) is dominated by the $\chi^{(3)}$ nonlinearity[7], which is also the dominant parametric nonlinearity in optical-fibre-based technology. Most previous $\chi^{(3)}$-based frequency conversion work in nanophotonic devices[8–14] has employed a degenerate or nondegenerate four-wave mixing (FWM) process called parametric amplification (PA), where idler generation goes along with vacuum noise amplification in a system with anomalous dispersion at the pump wavelength. While PA-based frequency conversion works well for many classical applications (see Supplementary Section I for more discussion), there is a fundamental theoretical limit on the achievable signal-to-noise ratio (SNR) for the converted idler at a single-photon-level input, limiting its application for QFC[15]. Alternatively, there is a non-degenerate FWM process, termed four-wave-mixing Bragg scattering (FWM-BS)[16–18], that is typically operated in the normal dispersion regime and does not amplify vacuum fluctuations. As a result, FWM-BS can in principle be noiseless, and in fact its Hamiltonian has the form of a state transfer process and can be considered as an active beam splitter[18]. In addition, PA does not allow an arbitrary choice of the target conversion wavelength, which can be important for both the aforementioned classical and quantum applications. In contrast, FWM-BS provides a controllable spectral translation set by the difference in pump frequencies[16,19]. While two earlier works demonstrated FWM-BS in nanophotonic waveguides, the efficiency was $\lesssim 5$ %, despite the use of short pulsed pumps with a peak power of a few Watts[20,21]. Recent theoretical works [22,23] indicate a rising interest in developing FWM-BS using a microresonator structure, in order to achieve efficient single-photon-level frequency conversion with a reasonable power budget.

In this Article, we show for the first time a resonance-enhanced FWM-BS process, using a compact Si_3N_4 microring resonator that significantly reduces the required pump power (< 60 mW continuous-wave pumps). The 1550 nm band and 980 nm band are considered due to their relevance to low-loss transmission through optical fibres and quantum light generation by InAs/GaAs quantum dots, respectively. We first show efficient (> 25 % conversion efficiency) 980 nm intraband frequency conversion with spectral translation over a few nanometers, which can be used to achieve indistinguishability between InAs/GaAs quantum dots emitting with slightly different wavelengths[24]. Then, we demonstrate wideband frequency conversion from the 1550 nm band to the 980 nm band (upconversion) and the 980 nm band to the 1550 nm band (downconversion), with each showing > 60 % conversion efficiency. The background noise properties for both 980 nm intraband conversion and wideband 980 nm to 1550 nm downconversion are studied using single-photon-level inputs. The performance level of our nanophotonic frequency conversion interfaces (in terms of conversion efficiency and SNR) is comparable to more mature $\chi^{(3)}$ technology such as highly nonlinear and photonic crystal fibres[4,25,26], while typically operating with much lower power, continuous-wave optical pumps (see Supplementary Section II). Moreover, the compact geometry, scalable fabrication process, and versatility make them a promising resource for future applications.

Results

System Design The silicon nitride (Si_3N_4) photonic platform supports many ingredients needed for efficient and low power microresonator frequency conversion, including high Q modes across a wide wavelength span, negligible nonlinear absorption at the pump wavelengths due to the wide bandgaps of Si_3N_4 and SiO_2 (unlike Si), a large nonlinear refractive index (10x higher than SiO_2), and the ability to use geometry to engineer dispersion and achieve phase matching[7]. These features, critical in the development of Kerr microresonator frequency combs[7,11,27,28], underpin our work, though there are a number of specific considerations for FWM-BS, which we outline below.

We use a 40 μm radius microring resonator (Figs. 1a-b) to implement FWM-BS, with the fabrication details provided in the Methods. The first FWM-BS scheme under study is illustrated in Fig. 1c, where the interference of two 1550 nm band pumps effectively creates a grating in the Si_3N_4 $\chi^{(3)}$ nonlinear medium that scatters the 980 nm input signal to two idlers, which are separated from the signal by an amount equal to the difference in pump frequencies. These two

idlers are labeled as $i-$ and $i+$ ($i+$ denotes the idler with higher frequency), similar to the Stokes and anti-Stokes sidebands in Raman scattering. In whispering-galley-mode geometries, phase matching is satisfied by the correct choice of azimuthal mode numbers, while energy conservation has to be met through careful engineering. The conversion efficiencies for $i\pm$ are a function of their frequency detunings with respect to their corresponding cavity modes, which can be derived as $\delta\hat{\omega}_{\pm} \approx (\hat{\omega}_{i\pm} - \hat{\omega}_s) \mp |\hat{\omega}_{p1} - \hat{\omega}_{p2}|$ (see Supplementary Section III.A), where $\hat{\omega}_{p1,p2,s,i\pm}$ denotes the resonance frequency accommodating pump 1, pump 2, signal s, and idler $i_{\pm}$, respectively. The resonance frequencies in each band can be approximated by the Taylor series $\hat{\omega}_{\mu} = \hat{\omega}_0 + D_1\mu + \frac{1}{2}D_2\mu^2 + \frac{1}{6}D_3\mu^3...$, where $\hat{\omega}_0$ is the reference frequency, $D_1/2\pi$ is the free spectral range (FSR) of the resonator at $\hat{\omega}_0$, D_n $(n = 2,,3...)$ are parameters characterizing the resonance dispersion, and μ is an integer representing the relative mode order number with respect to $\hat{\omega}_0$. As a result, the frequency detuning for $i\pm$ corresponding to pump separation of $|\mu|$ FSRs is given by $\delta\hat{\omega}_{\pm|\mu|} \approx \pm\delta D_1|\mu| + \frac{1}{2}\delta D_{2,\mp}\mu^2...$, where $\delta D_1 \equiv D_1^{980} - D_1^{1550}$ and $\delta D_{2,\pm} \equiv D_2^{980} \pm D_2^{1550}$, with the 980 and 1550 superscripts marking the reference wavelengths in the 980 nm and 1550 nm bands, respectively. The first order frequency matching condition ($\delta D_1 \approx 0$) is satisfied by using a ring waveguide geometry that exhibits $n_g^{1550} = n_g^{980}$ (Fig. 2a), where n_g stands for the group index and is inversely proportional to the FSR. Moreover, it is important to be in the overcoupled regime for the 980 nm band to extract the generated idlers efficiently while maintaining a reasonably high Q in the 1550 nm band for resonance enhancement. Conventional point coupling, which relies upon the evanescent field overlap between the modes of a straight waveguide and the resonator, presents difficulty in doing so since the coupling becomes significantly weaker at shorter wavelengths (Fig. 2b). This problem is solved here by implementing the pulley coupling scheme[29–31], which has an increased interaction length (Fig. 1b) and thus the coupling Q depends on both the evanescent field overlap and phase matching. Because the resonant modes in the 1550 nm band extend further outside the ring core than in the 980 nm band, resulting in larger mode overlap, we choose an access waveguide width that is phase matched (mismatched) to the resonant modes in the 980 nm (1550 nm) band, resulting in similar Q values in the two bands. This is demonstrated by the simulation result in Fig. 2b, and confirmed by linear transmission measurements of the fabricated devices. By varying the coupling parameters (gap and coupling length) across multiple devices, we find a device operating in the overcoupled regime in both the 1550 nm and 980 nm bands, with loaded Q values $\approx 1.5 \times 10^5$ (linewidth $\kappa/2\pi \approx 1.29$ GHz) and 2.4×10^5 ($\kappa/2\pi \approx 1.28$ GHz), respectively (Fig. 2c-d). In addition, with the aid of a 200 MHz resolution wavemeter, the

resonances in each band can be measured (Fig. 2e-f), from which we extract $D_1^{1550}/2\pi = 572.39$ GHz $\pm$ 0.05 GHz and $D_1^{980}/2\pi = 572.25$ GHz $\pm$ 0.05 GHz, where the uncertainty is due to the wavemeter resolution and represents a one standard deviation value. The difference in FSR between the 1550 nm and 980 nm bands is well below the resonator linewidth, indicating the first order frequency matching condition has been satisfied. We also extract high-order dispersion terms D_2 and D_3 in the two wavelength bands of interest and find that the resonator shows normal dispersion ($D_2 < 0$) in both bands. In general, D_2 and D_3 need to be taken into account for the frequency detuning calculation of idlers when the two pumps are widely separated, as the deviation of resonance frequencies from an equally spaced frequency grid (separated by one FSR) becomes comparable to the resonance linewidth for large $|\mu|$ values.

980 **nm intraband conversion.** The experimental setup is shown in Fig. 3a, where the two 1550 nm pumps are amplified and combined with the 980 nm signal, and coupled to the chip using a lensed fibre (coupling loss $\approx$ 5.5 dB and 6.5 dB per facet for the 1550 nm and 980 nm band, respectively). To tune both pump lasers into resonance, narrowband filters (bandwidth $\approx$ 1 nm) are placed in front of each 1550 nm detector to select each pump while it scans across its resonance with decreasing frequency detuning, showing a characteristic triangular resonance shape from a combined Kerr-nonlinear and thermal resonance shift[32]. As we reduce the spectral distance between one pump and its nearby resonance, the intracavity power rises and the dominant thermal shift sends all the resonances towards lower frequencies, effectively increasing the spectral distance of the other pump laser with respect to its accommodating resonance. Therefore, it is necessary to tune the two pump lasers in an interactive and iterative way until both are thermally locked on their respective resonances.

Once the pumps are thermally locked, we characterize the frequency conversion process through two types of measurements. The first spectrally resolves the light exiting the chip using an optical spectrum analyzer (OSA). The second examines signal depletion and idler generation by swept wavelength spectroscopy of the signal resonance. Figure 3b shows the experimental results when the two pumps are separated by one FSR and of nearly equal power. When the pump power is low (first column, case I), only two small sidebands ($i+$ and $i-$) are observed in the 980 nm spectrum (second column, case I); as the pump power increases (case II), secondary pump peaks appear in the 1550 nm spectrum from pump mixing, which in turn generate higher-order idlers in the 980 nm spectrum. The on-chip conversion efficiency, defined as the converted idler photon flux

at the waveguide output divided by the input signal photon flux at the waveguide input, reaches a maximum of -6.2 dB for each of $i+$ and $i-$ at 16 mW power per pump (case III). In addition, multiple high-order idlers are generated, though the red idlers decrease more rapidly than the blue ones due to an accidental mode shift of the 978 nm resonance (Fig. 2f, $\mu = -2$) caused by mode interactions (see Supplementary Section V). If we further increase the pump power (case IV), more sidebands are observed in both the 1550 nm and 980 nm bands, but the conversion efficiency for $i+$ and $i-$ slightly decreases, indicating there is a saturation level for a specific idler. The OSA data is complemented by transmission measurements in the 980 nm band (third column). First, we use a narrowband filter (centered on the signal resonance with bandwidth ≈ 0.4 nm) to reject all of the generated idlers and provide a measurement of the signal transmission. As the pump power increases, the signal resonance evolves from overcoupled (cases I and II) to critically coupled (case III) and then undercoupled (case IV), indicating an increased intrinsic loss that is attributed to signal depletion due to the frequency conversion process. In addition, mode splitting starts to appear as the pump power increases, a phenomenon expected when there is a strong coupling between the signal and adjacent idlers (see next section and also Supplementary Section III.A). Next, we remove the narrowband filter and directly detect light in the whole 980 nm band. At low pump powers (cases I and II), the transmission scan is the same as the linear case, but when the conversion efficiency is high (cases III and IV), the extinction ratio becomes much smaller, suggesting a significant amount of idler generation when the signal is on-resonance. Moreover, mode splitting is also evident at sufficiently high powers (case IV). We can also increase the separation between the two pumps. When they are separated by 5 FSRs (Fig. 3c), the optimum on-chip conversion efficiency for $i+$ and $i-$ is similar to the 1 FSR case, indicating the frequency matching condition is well satisfied. Thus, in this configuration, frequency conversion with a signal translation as low as 1.8 nm (1 FSR) and as large as 9.0 nm (5 FSR) can be achieved with an efficiency as high as 25 % in each first-order idler. In addition, if we count all the converted idlers, the total conversion efficiency is around 58% (case III in Fig. 2b), which can be shown to be limited by the intrinsic loss of the resonator (Supplementary Section II).

Numerical simulations Four-wave mixing in $\chi^{(3)}$ resonators can be described by the Lugiato-Lefever equation (LLE), a version of the nonlinear Schrodinger equation that includes driving and dissipation and which has been successfully applied to study microcavity frequency combs[33]. To understand our experimental results, numerical simulations based on a modified form of the

conventional LLE formalism are carried out. The modification is needed for FWM-BS to allow for three independent inputs[34] (i.e., two pumps and one signal). In addition, coupled mode equations are also used[35,36]. Though the two approaches are essentially equivalent[37,38], they differ in detailed forms and numerical implementation, which may render one better than the other depending on the scope of the problem. For example, the coupled mode equations are usually preferred for revealing the underlying physics, while the LLE method is capable of capturing all relevant physical mechanisms by automatically including a complete set of modes into simulation.

Figure 4a shows the simulation results based on the modified LLE method (see Methods and Supplementary Section III) for the case of 16 mW power per pump. Compared to the corresponding experimental results (Fig. 3b case III), we find the modified LLE simulation successfully models the pump mixing in the 1550 nm band and the multiple idler generation in the 980 nm band (Fig. 4b). In addition, there is a small noise band in the anomalous dispersion region (1100 nm to 1300 nm), which arises from modulation instability processes (i.e., one photon from the 980 nm signal and one photon from the 1550 nm pumps are converted to nearly degenerate photon pairs near the wavelength of 1200 nm), though such processes are generally frequency-mismatched and small enough to be neglected. The transmission scan of the signal resonance from the LLE simulation (Fig. 4c, left) also shows good agreement with the experimental data, and the observed mode splitting is explained by a simplified set of coupled mode equations to result from strong couplings induced by FWM-BS between the signal and its adjacent idlers (Supplementary Section III.A). Generally, increasing pump powers leads to larger mode splitting and increased conversion bandwidth for the signal photon (Fig. 4c, right), but not necessarily higher conversion efficiency for a specific idler as its conversion efficiency will eventually saturate.

SNR measurement Along with conversion efficiency, a key metric for quantum photonic applications (as well as some classical applications) is the background noise generated in the converted idler band. In general, one may expect that noise to originate due to the presence of strong pump fields, which through processes such as Raman scattering, may generate photons that are either directly resonant with the converted idler, or are resonant with the input signal and get frequency converted together with it. One advantage of the scheme presented here is that the signal and idler are about 600 nm away from the strong pump fields (and are on their anti-Stokes side), suggesting that noise due to Raman scattering should be limited.

To determine the suitability of this system as a QFC interface, we consider the conversion efficiency and SNR for an input signal at the single photon level ($\approx$ 1 pW, corresponding to photon flux $\approx 5 \times 10^6$ s^{-1}, which is consistent with the photon flux produced by systems such as a quantum dot single photon source[39] triggered at 50 MHz and with a source efficiency of 10 %). A single-photon avalanche diode (SPAD) is used to measure the power in the converted idler band, which is spectrally isolated from the 1550 nm pumps using a WDM and a 0.4 nm bandwidth bandpass filter (Fig. 3a). In addition, we have observed a small second harmonic signal from the 1550 nm pumps at 780 nm (Supplementary Section VIII), which we remove with a 930 nm longpass filter. The on-chip conversion efficiency, background noise power, and SNR are determined from knowledge of the coupling loss and insertion losses of the filtering elements. As shown in Fig. 4d, the on-chip conversion efficiency as a function of pump power for the $i+$ idler agrees with the LLE simulation, and peaks at $\approx$ 25 %. We next measure the noise power by turning off the input signal and considering two cases, when the pumps are on-resonance with their respective cavity modes and when they are off-resonance (Fig. 4e). Off resonance, any measured noise is found to be broadband emission from the erbium-doped fibre amplifier (EDFA) used for the pump, and can be significantly reduced by filtering at the input side, prior to the chip (see Fig. 3a, WDM filter placed after the EDFA). On resonance, we observe noise above the EDFA-determined background, at the level of a few fW. This noise is mainly contributed by the Si_3N_4 microresonator, though its origin is still under investigation (see Supplementary Section VIII). At the optimum conversion efficiency (25 % at pump power $\approx$ 16 mW), the SNR is larger than 80 : 1 for the aforementioned input signal photon flux $\approx 5 \times 10^6$ s^{-1}. Moreover, for triggered sources, we only need to consider generated noise that temporally coincides with the single photon emission, which is produced at well defined times (the triggering times) and over well defined intervals (the spontaneous emission lifetime; typically $\approx$ 1 ns for an InAs/GaAs quantum dot[39]). Therefore, either gated detection or temporal gating of the signal via amplitude modulation[40] can be used, with a typical duty cycle of 5 % (for a 50 MHz triggering rate). Since the measured background noise comes from a continuous-wave pump, we expect the corresponding noise level in the gated case to be reduced by a factor equal to the duty cycle, which will push the SNR to $> 1000 : 1$ at the optimum conversion efficiency.

Telecommunications band frequency conversion interface In addition to frequency conversion within the 980 nm band, we can use the same device for frequency conversion between the 1550 nm and 980 nm bands. As illustrated by Figs. 5a and 5c, with one pump in each band, the signal

can be upconverted (downconverted) from the 1550 nm (980 nm) band to the 980 nm (1550 nm) band. Although the pump power available from our 980 nm laser is limited (maximum ≈ 8 mW), it can be compensated by using a relatively strong pump in the 1550 nm band, since the conversion efficiency is determined by the product of the two pump powers[17]. Figure 5b shows one example of upconversion, measured using the experimental setup shown in Fig. S8a of the Supplementary Material, where the signal is separated from the 1550 nm pump by 8 FSRs (i.e., $\mu = 8$). In the 980 nm band spectrum, the converted blue idler ($i+$) shows a conversion efficiency ≈ -2.2 dB while the red idler ($i-$) is much weaker (as in the 980 nm intraband case, we define conversion efficiency in terms of photon flux). The difference in the conversion efficiency indicates different frequency detunings for the two idlers, which is expected as high-order dispersion terms become important when $|\mu|$ is large (see Supplementary Section VI for more detailed discussions). In addition, we find the amplified spontaneous emission (ASE) around the 1550 nm pump (largely due to the EDFA) is also upconverted to the 980 nm band (small peaks around the 980 nm pump). By adding a narrowband filter after the EDFA, the ASE of the 1550 nm pump can be suppressed.

As one would expect, if efficient 1550 nm to 980 nm upconversion can be achieved in this system, efficient 980 nm to 1550 nm downconversion should also be achievable, and easily measured by simply moving the input signal to the 980 nm band (Fig. 5c). Figure 5d shows a representative downconversion spectrum when the separation between the input signal and the 980 nm band pump is 7 FSRs ($\mu = 7$), where in this case a narrowband ASE rejection filter surrounding the 1550 nm pump is applied (see Supplementary Fig. S9a). Along with a conversion efficiency for $i+$ that is similar to the upconversion case (≈ -2.8 dB), we see the ASE rejection filter has successfully suppressed the spurious peaks present in the upconversion spectrum.

To further explore the properties of wideband frequency conversion based on the FWM-BS scheme, we focus on the downconversion case by varying the signal position in the 980 nm band while keeping pump powers in the 1550 nm and 980 nm band ≈ 50 mW and 8 mW, respectively (Fig. 6a). As we increase the separation between the signal and the 980 nm pump (i.e., μ increases), the blue idler $i+$ moves away from the 1550 nm pump by an equal amount of frequency shift with slowly decreasing power. By contrast, the red idler $i-$ shows slightly worse conversion efficiency than $i+$ when μ is small, but as μ increases its power decreases much more rapidly. Their different performance can be understood by calculating the corresponding frequency detunings (Fig. 6a inset, right), which reveal that $i+$ has a small frequency detuning for up to 22 FSR separation from the 1550 pump, while the frequency detuning for $i-$ is already comparable to the resonance

linewidth after 5 FSRs. In Fig. 6b, the conversion efficiencies for both $i+$ and $i-$ are extracted from Fig. 6a (markers), and agree with the simulation results based on coupled mode equations (solid lines, see Supplementary Section III.B). With less than 60 mW total pump power, the maximum conversion efficiency for $i+$ is measured to be $\approx$ 60 % (-2.2 dB), and the spectral range over which the input signal can be tuned without reducing the conversion efficiency by more than 3 dB (i.e., conversion efficiency $>$ 30 %) is estimated to be nearly 8.2 THz. Even when the signal is 13 THz away from the 980 nm pump, the conversion efficiency for $i+$ is still more than 10 %. As discussed in Supplementary Sections I and II, more efficient out-coupling of the frequency-converted photons generated within the ring into the access waveguide is the primary improvement needed to push the conversion efficiencies higher. An efficiency as high as 85% is predicted for a frequency-matched downconversion process if the intrinsic Q can be increased to 2×10^6 while maintaining a coupling Q around 2×10^5.

To measure the SNR level for the wideband frequency conversion (see Supplementary Section VIII), we turn off the signal and measure the noise at the idler frequency while keeping the pumps on. Narrowband filters are added at the input side for each pump to suppress its ASE level so that the single-photon-level signal and idlers are not overwhelmed by the ASE noise. For the upconversion case as shown in Fig. 5a, the 1550 nm pump is expected to generate little noise in the 980 nm band as already demonstrated in the 980 nm intraband frequency conversion (Fig. 4e), although it is not trivial to suppress the 980 nm pump to sub pW level on the detection side ($>$ 100 dB suppression) so that single-photon-level noise can be measured. For the downconversion case, the noise is found to be mostly from the 1550 nm pump and the contribution of the 980 nm pump is much smaller. At the output, after filtering out the 1550 nm pump, the transmitted light goes through a narrowband filter with a tunable bandwidth (32 pm to 600 pm) and center wavelength (1460 nm to 1560 nm) before detection by a SPAD. When the 1550 nm pump is off-resonance, the noise power scales with the filtering bandwidth and exhibits a smooth spectral response as we shift the center wavelength of the filter, indicating it is a broadband noise. On the other hand, when we tune the pump into resonance, the detected noise initially stays the same if the narrowband filter is out of resonance, but increases significantly if the filter is centered on the idler resonance. The increased noise power changes little as we adjust the filtering bandwidth, suggesting this portion of noise is resonant. Figure 6c shows the measured on-chip noise power for idlers with different spectral separation from the 1550 nm pump (power fixed $\approx$ 50 mW). The pump-off-resonance noise is identified as anti-Stokes Raman scattering generated inside fibre

after the EDFA, as the noise is almost the same if we remove the chip and introduce a similar insertion loss between two lensed fibres (see Supplementary Section VIII for more details). On the other hand, the resonant noise (i.e., noise generated at the idler frequency with bandwidth limited by the cavity linewidth) for the pump-on-resonance case is believed to be from the Si_3N_4 microresonator, and decreases rapidly as the idler moves away from the pump (Supplementary Section VIII presents measurements of the noise spectra in the 1460 nm to 1620 nm band and a discussion of its possible origin). For example, the resonant noise is measured to be ≈ 8 pW for the $\mu = 7$ idler (1528 nm resonance). Assuming the input signal is from a single photon emitter with a photon flux $\approx 5 \times 10^6$ s^{-1} (≈ 1 pW power), the converted blue idler has a power ≈ 0.52 pW (≈ -2.8 dB conversion efficiency). At first glance, it seems the signal will be overwhelmed by the noise. However, just as we discussed in the intraband conversion case, for a triggered single photon source, either gated detection or temporal gating of the light exiting the frequency conversion device can be used, with a typical duty cycle of 5 %. This will improve the SNR to be more than unity under current conditions. Another straightforward route to reducing the noise power is to design a frequency-matched idler that has a larger spectral separation from the pump. Improving the Si_3N_4 material quality may also be important, as the resonant noise is suspected to be correlated with the significant material absorption inferred by a relatively large thermo-optic shift for the pump modes in the 1550 nm band. Figure 6d shows that for a fixed idler ($\mu = 7$ at 1528 nm), the pump-off-resonance noise has a linear dependence on the pump power while the resonant noise is clearly nonlinear. Since the conversion efficiency is determined by the product of two pump powers, and the 980 nm pump generates little noise in the 1550 nm band due to the large spectral separation (Supplementary Section VIII), it seems possible to improve the SNR dramatically by using a relatively large 980 nm pump (e.g., 40 mW) and a smaller 1550 nm pump (e.g., 10 mW). Optimizing the noise performance of this downconversion interface will be a subject of future studies.

Discussion

We have demonstrated efficient single-photon-level frequency conversion through four-wave-mixing Bragg scattering (FWM-BS) in monolithic Si_3N_4 microring resonators. In contrast to parametric amplification (PA), which is the basis of most prior work in Kerr-based nanophotonic devices[7], FWM-BS avoids spontaneous emission noise and can be, in principle, noiseless[18]. We have demonstrated background noise powers in the fW to pW range, and potential routes to reduce this further have been identified. The performance of these devices is already comparable to what

has been demonstrated for FWM-BS in highly nonlinear fibres and photonic crystal fibres and in some respects, such as pump power required and extent of the spectral translation range, exceeds them (see Supplementary Section II for a more detailed comparison). Moreover, the versatility of the FWM-BS process has been demonstrated. Because the frequency translation range is set by the difference in pump frequencies (in contrast to frequency conversion by either PA or the $\chi^{(2)}$ nonlinearity), our devices enable both intraband conversion (translation range between 1.8 nm and 9.0 nm shown with no degradation in performance) and interband conversion (upconversion and downconversion over a translation range >560 nm). These devices are already suitable for proof-of-principle QFC experiments with single photon Fock states, and the concepts we utilize - dispersion engineering to ensure frequency matching and tailored waveguide coupling to ensure efficient injection of the signal and pumps and extraction of the converted idler - can be readily applied to connect visible-wavelength quantum light sources (e.g., based on colour centers in diamond or trapped atoms and ions) with the telecommunications band.

There are several topics to be addressed in the pursuit of such goals. The use of a resonantly-enhanced process comes at the expense of bandwidth, which is largely determined by the cavity linewidth $\kappa/2\pi \approx 1.3$ GHz in both the 980 nm and 1550 nm bands (at peak conversion efficiency, the bandwidth broadens to > 2.8 GHz as shown in Fig. 4c). Importantly, this bandwidth is large enough to accommodate the photons generated by single InAs/GaAs quantum dots[39], our intended target application, and recently demonstrated quantum light sources in the Si_3N_4 platform [41,42] and similar wide bandgap dielectrics [43] would also be compatible, as would a host of the aforementioned single quantum emitter systems, if the dispersion is engineered to accommodate their specific transition wavelengths. The GHz bandwidth stands in contrast to compact wavelength converters based on cavity optomechanics[44–46], which have been limited to the MHz range (at most). Nevertheless, even with a sufficiently large bandwidth, the precise temporal profile of the incoming photon's wavepacket is an important consideration when determining the efficiency with which it can be coupled into the frequency conversion cavity[47,48]. More generally, bandwidth and temporal shaping to efficiently load the cavity are topics that will need to be considered when moving from frequency conversion of continuous-wave signals to pulsed light. Finally, while the focus of our discussion has been on the demanding application of QFC, the potential classical applications of this work are also significant. This includes add-drop wavelength multiplexing and cross-connect switching that utilize the interband FWM-BS process, and spectral translation of signals across hundreds of nanometers to connect, for example, atomic frequency references with

telecommunications-band signals.

Methods

Device fabrication First, the layer stack is created by low-pressure chemical vapor deposition of a 480 nm thick Si_3N_4 layer on top of a 3 μm thick SiO_2 layer, which in turn was grown via thermal oxidation of a 100 mm Si wafer. The wavelength-dependent refractive index and thickness of the layers are determined using a spectroscopic ellipsometer, with the data fit to an extended Sellmeier model. After dicing into chips, the microring-waveguide devices are created by electron-beam lithography of a negative tone resist, followed by reactive ion etching of the Si_3N_4 using a CF_4/CHF_3 chemistry, removal of deposited polymer and remnant resist, and annealing at 1150 °C in an O_2 environment for 3 hours.

Numerical simulation The simulations presented in this work are based on coupled mode equations as well as a modified LLE method. For the 980 nm intraband conversion, we first study a simplified set of coupled mode equations (which neglects pump mixing in the 1550 nm band and high-order idler generation in the 980 nm band) to gain some physical insight (Supplementary Section III.A), from which the mode splitting observed in the experiment (Fig. 3b, case IV) can be easily understood. Next, a modified LLE method is developed (Supplementary Section III.C), which is essentially a systematic way to implement the same coupled mode equations by including a complete set of resonant modes. The simulation results shown in Figs. 4a and 4c show good agreement between the LLE simulation and the experimental results, indicating it has captured all relevant physical mechanisms. As for the wideband frequency conversion between the 1550 nm and 980 nm bands, since the pump mixing is absent, the LLE method is expected to generate almost the same results as the coupled mode equations. We use the coupled mode equations to study the device's performance, as its numerical computation is much faster than the LLE method (Supplementary III.B). Additional discussions on upconversion and the effect of pump detunings on the frequency conversion process are also provided in the Supplementary Material (Section VI).

Frequency conversion metrics We characterize our frequency conversion devices based on their on-chip conversion efficiency, noise power, signal-to-noise ratio for a single-photon-level input, and required pump power. The on-chip conversion efficiency is defined as the ratio of a given idler's photon flux at the coupling waveguide output to the signal photon flux at the coupling waveguide input. The background noise power is defined as the power at a given idler's spectral position taken over a specified bandwidth (determined by a narrowband filter) and with the input signal switched off and both pumps turned on. The SNR for single-photon-level inputs is estimated by attenuating the input signal level to a photon flux consistent with

that achieved by quantum dot single photon sources (e.g., 1 pW $\approx 5\times10^6$ s^{-1}), and measuring the photon flux in a given idler band with both the signal on and off. Finally, the pump powers listed are on-chip and at the waveguide input.

---

* Electronic address: qing.li@nist.gov

† Electronic address: kartik.srinivasan@nist.gov

[1] Boyd, R. W. *Nonlinear Optics* (Academic press, 2003).

[2] Agrawal, G. P. *Nonlinear Fiber Optics* (Academic Press, Amsterdam, 2007).

[3] Langrock, C. *et al.* Highly efficient single-photon detection at communication wavelengths by use of upconversion in reverse-proton-exchanged periodically poled linbo$_3$ waveguides. *Opt. Lett.* **30**, 1725–1727 (2005).

[4] Gnauck, A. H., Jopson, R., McKinstrie, C., Centanni, J. & Radic, S. Demonstration of low-noise frequency conversion by Bragg scattering in a fiber. *Opt. Express* **14**, 8989–8994 (2006).

[5] Kumar, P. Quantum Frequency-Conversion. *Opt. Lett.* **15**, 1476–1478 (1990).

[6] Raymer, M. G. & Srinivasan, K. Manipulating the color and shape of single photons. *Phys. Today* **65**, 32–37 (2012).

[7] Moss, D. J., Morandotti, R., Gaeta, A. L. & Lipson, M. New cmos-compatible platforms based on silicon nitride and hydex for nonlinear optics. *Nature Photon.* **7**, 597–607 (2013).

[8] Foster, M. A. *et al.* Broad-band optical parametric gain on a silicon photonic chip. *Nature* **441**, 960–963 (2006).

[9] DelHaye, P. *et al.* Optical frequency comb generation from a monolithic microresonator. *Nature* **450**, 1214–1217 (2007).

[10] Turner, A. C., Foster, M. A., Gaeta, A. L. & Lipson, M. Ultra-low power parametric frequency conversion in a silicon microring resonator. *Opt. Express* **16**, 4881–4887 (2008).

[11] Levy, J. S. *et al.* CMOS-compatible multiple-wavelength oscillator for on-chip optical interconnects. *Nature Photon.* **4**, 37–40 (2010).

[12] Razzari, L. *et al.* Cmos-compatible integrated optical hyper-parametric oscillator. *Nature Photon.* **4**, 41–45 (2010).

[13] Liu, X., Osgood, R. M., Vlasov, Y. A. & Green, W. M. Mid-infrared optical parametric amplifier using silicon nanophotonic waveguides. *Nature Photon.* **4**, 557–560 (2010).

[14] Zlatanovic, S. *et al.* Mid-infrared wavelength conversion in silicon waveguides using ultracompact telecom-band-derived pump source. *Nature Photon.* **4**, 561–564 (2010).

[15] McKinstrie, C., Yu, M., Raymer, M. & Radic, S. Quantum noise properties of parametric processes. *Opt. Express* **13**, 4986–5012 (2005).

[16] Marhic, M. E., Yang, F., Kazovsky, L. & Park, Y. Widely tunable spectrum translation and wavelength exchange by four-wave mixing in optical fibers. *Opt. Lett.* **21**, 1906–1908 (1996).

[17] Uesaka, K., Kin-Yip, K., M.E., Marhic & Kazovsky, L. Wavelength exchange in a highly nonlinear dispersion-shifted fiber: Theory and experiments. *IEEE J. Sel. Top. Quan. Elec.* **8**, 560–568 (2002).

[18] McKinstrie, C., Harvey, J., Radic, S. & Raymer, M. Translation of quantum states by four-wave mixing in fibers. *Opt. Express* **13**, 9131–9142 (2005).

[19] Lefrancois, S., Clark, A. S. & Eggleton, B. J. Optimizing optical bragg scattering for single-photon frequency conversion. *Phys. Rev. A* **91**, 013837 (2015).

[20] Agha, I., Davanço, M., Thurston, B. & Srinivasan, K. Low-noise chip-based frequency conversion by four-wave-mixing bragg scattering in sin x waveguides. *Opt. Lett.* **37**, 2997–2999 (2012).

[21] Agha, I., Ates, S., Davanço, M. & Srinivasan, K. A chip-scale, telecommunications-band frequency conversion interface for quantum emitters. *Opt. Express* **21**, 21628–21638 (2013).

[22] Huang, Y., Velev, V. & Kumar, P. Quantum frequency conversion in nonlinear microcavities. *Opt. Lett.* **38**, 2119–2121 (2013).

[23] Lin, Z., Johnson, S. G., Rodriguez, A. W. & Loncar, M. Design of diamond microcavities for single photon frequency down-conversion. *Opt. Express* **23**, 25279–25294 (2015).

[24] Ates, S. *et al.* Two-Photon Interference Using Background-Free Quantum Frequency Conversion of Single Photons Emitted by an InAs Quantum Dot. *Phys. Rev. Lett.* **109**, 147405 (2012).

[25] McGuinness, H. J., Raymer, M. G., McKinstrie, C. J. & Radic, S. Quantum frequency translation of single-photon states in a photonic crystal fiber. *Phys. Rev. Lett.* **105**, 093604 (2010).

[26] Clark, A. S., Shahnia, S., Collins, M. J., Xiong, C. & Eggleton, B. J. High-efficiency frequency conversion in the single-photon regime. *Opt. Lett.* **38**, 947–949 (2013).

[27] Ferdous, F. *et al.* Spectral line-by-line pulse shaping of on-chip microresonator frequency combs. *Nature Photon.* **5**, 770–776 (2011).

[28] Brasch, V. *et al.* Photonic chip–based optical frequency comb using soliton cherenkov radiation. *Science* **351**, 357–360 (2016).

[29] Chin, M. & Ho, S. Design and modeling of waveguide-coupled single-mode microring resonators. *J.*

Lightwave Technol. **16**, 1433 (1998).

[30] Shah Hosseini, E., Yegnanarayanan, S., Atabaki, A. H., Soltani, M. & Adibi, A. Systematic design and fabrication of high-q single-mode pulley-coupled planar silicon nitride microdisk resonators at visible wavelengths. *Opt. Express* **18**, 2127–2136 (2010).

[31] Spencer, D. T., Bauters, J. F., Heck, M. J. & Bowers, J. E. Integrated waveguide coupled si3n4 resonators in the ultrahigh-q regime. *Optica* **1**, 153–157 (2014).

[32] Carmon, T., Yang, L. & Vahala, K. Dynamical thermal behavior and thermal self-stability of microcavities. *Opt. Express* **12**, 4742–4750 (2004).

[33] Coen, S., Randle, H. G., Sylvestre, T. & Erkintalo, M. Modeling of octave-spanning kerr frequency combs using a generalized mean-field lugiato–lefever model. *Opt. Lett.* **38**, 37–39 (2013).

[34] Hansson, T. & Wabnitz, S. Bichromatically pumped microresonator frequency combs. *Phys. Rev. A* **90**, 013811 (2014).

[35] Matsko, A. B., Savchenkov, A. A., Strekalov, D., Ilchenko, V. S. & Maleki, L. Optical hyperparametric oscillations in a whispering-gallery-mode resonator: Threshold and phase diffusion. *Phys. Rev. A* **71**, 033804 (2005).

[36] Chembo, Y. K. & Yu, N. Modal expansion approach to optical-frequency-comb generation with monolithic whispering-gallery-mode resonators. *Phys. Rev. A* **82**, 033801 (2010).

[37] Hansson, T., Modotto, D. & Wabnitz, S. On the numerical simulation of kerr frequency combs using coupled mode equations. *Opt. Commun.* **312**, 134–136 (2013).

[38] Chembo, Y. K. & Menyuk, C. R. Spatiotemporal lugiato-lefever formalism for kerr-comb generation in whispering-gallery-mode resonators. *Phys. Rev. A* **87**, 053852 (2013).

[39] Michler, P. *Single Semiconductor Quantum Dots* (Springer Verlag, Berlin, 2009).

[40] Ates, S. *et al.* Improving the performance of bright quantum dot single photon sources using temporal filtering via amplitude modulation. *Sci. Rep.* **3** (2013).

[41] Dutt, A. *et al.* On-chip optical squeezing. *Phys. Rev. Appl.* **3**, 044005 (2015).

[42] Ramelow, S. *et al.* Silicon-nitride platform for narrowband entangled photon generation. *arXiv:1508.04358* (2015).

[43] Reimer, C. *et al.* Cross-polarized photon-pair generation and bi-chromatically pumped optical parametric oscillation on a chip. *Nature Commun.* **6**, 8236 (2015).

[44] Dong, C., Fiore, V., Kuzyk, M. C. & Wang, H. Optomechanical dark mode. *Science* **338**, 1609–1613 (2012).

[45] Hill, J. T., Safavi-Naeini, A. H., Chan, J. & Painter, O. Coherent optical wavelength conversion via cavity optomechanics. *Nature Commun.* **3**, 1196 (2012).

[46] Liu, Y., Davanço, M., Aksyuk, V. & Srinivasan, K. Electromagnetically induced transparency and wideband wavelength conversion in silicon nitride microdisk optomechanical resonators. *Phys. Rev. Lett.* **110**, 223603 (2013).

[47] Bader, M., Heugel, S., Chekhov, A. L., Sondermann, M. & Leuchs, G. Efficient coupling to an optical resonator by exploiting time-reversal symmetry. *New J. Phys.* **15**, 123008 (2013).

[48] Liu, C. *et al.* Efficiently loading a single photon into a single-sided fabry-perot cavity. *Phys. Rev. Lett.* **113**, 133601 (2014).

Acknowledgements Q.L. acknowledges support under the Cooperative Research Agreement between the University of Maryland and NIST-CNST, Award 70NANB10H193. The authors thank Jin Liu for help with using the grating spectrometer for the noise measurement, Lawrence Van Der Vegt from Yenista Optics for the loan of a 1550 nm tunable filter, and Scott Papp from NIST Boulder for helpful comments.

Author Contributions Q.L. led the design, fabrication, and measurement, with assistance from M.D. and K.S. Q.L. and K.S. wrote the manuscript, and K.S. supervised the project.

Additional Information Correspondence and requests for materials should be addressed to Q.L. and K.S.

Competing financial interests The authors declare no competing financial interests.

Figures

FIG. 1: **Principle of operation and device geometry**. **a**, Schematic of the microresonator geometry used, where an input signal s is converted to idlers $i+$ and $i-$ through application of two pump fields p_1 and p_2. **b**, Scanning electron micrograph of a 40 μm radius microring resonator, showing the pulley-coupled access waveguide. **c**, Schematic of the FWM-BS process for 980 nm intraband frequency conversion, where s, $i+$, and $i-$ are in the 980 nm band and the pumps p_1 and p_2 are in the 1550 nm band. Of critical importance to efficient conversion is the spectral matching of the frequency components generated by FWM-BS ($\omega_{s,i+,i-,p1,p2}$) with the resonant frequencies of the cavity modes ($\hat{\omega}_{s,i+,i-,p1,p2}$). As shown in Figs. 5-6, the same microring can be used to create a frequency conversion interface between the 980 nm and 1550 nm bands.

FIG. 2: **Device design, dispersion, and coupling characterization**. **a**, Simulated group index difference between the 1550 nm and 980 nm bands for various waveguide cross-sections with top air cladding and bottom oxide cladding (inset), from which a 1400 nm $\times$ 480 nm ring cross-section is chosen. **b**, Simulated coupling Q for a 820 nm wide waveguide coupled to the microring (gap = 250 nm), considering both point coupling and pulley coupling (coupling length = 25 μm). **c-d**, Linear transmission scan of the fabricated sample for the 1550 nm and 980 nm bands, with intrinsic/total quality factors $\approx 4.5\times10^5/1.5\times10^5$ and $9.0\times10^5/2.4\times10^5$, respectively. **e-f**, Deviation of the measured resonance frequencies (markers) from an equidistant frequency grid $\omega_0+\mu D_1$ for the 1550 nm and 980 nm bands, where $D_1^{1550}/2\pi = 572.39$ GHz $\pm$ 0.05 GHz and $D_1^{980}/2\pi = 572.25$ GHz $\pm$ 0.05 GHz (the displayed one standard deviation uncertainty is due to the wavelength resolution). The solid lines are fits using dispersion parameters $D_2/2\pi \approx -31.04$ MHz and $D_3/2\pi \approx 0.71$ MHz for the 1550 nm band, and $D_2/2\pi \approx -3.43$ MHz and $D_3/2\pi \approx -0.30$ MHz for the 980 nm band.

FIG. 3: 980 **nm intraband frequency conversion**. **a**, Experimental setup (OSA: optical spectrum analyzer). **b**, Results for two pumps separated by one free spectral range (FSR). The two pumps and the signal are located at 1550.6 nm, 1555.2 nm, and 974.4 nm, respectively. Four cases (I-IV) corresponding to different pump powers are displayed (the signal power is fixed at 45 μW): the first two columns show OSA spectra in the 1550 nm and 980 nm band, respectively, and the last column shows transmission scans of the signal around its thermally-shifted resonance (x-axis origin). The transmission data is taken both with a narrowband filter centered on the signal resonance (rejecting all converted idlers), and across the full 980 nm band (no filter). For cases I and II, these curves are identical. **c**, Experimental results for the two pumps separated by five FSRs (at 1541.5 nm and 1564.5 nm) and signal at 974.4 nm. In all 1550 nm band spectra, 0 dB is referenced to 1 mW.

FIG. 4: **Numerical simulations and SNR measurement for 980 nm intraband conversion.** **a**, (Bottom) Lugiato-Lefever equation simulation of the output waveguide spectrum for 16 mW power per pump and signal power of 0.1 pW. (Top) Dispersion parameter (980 nm and 1550 nm bands highlighted), obtained from an eigenmode solver and converted to an equivalent group velocity dispersion. **b**, zoomed-in 980 nm spectrum with the y-axis normalized to input photon flux. **c**, Simulated transmission scan of the signal resonance (left) and on-chip conversion efficiency for $i+$ (right) for several pump powers. The x-axis is wavelength detuning normalized by the resonance linewidth ($2\Delta\lambda \approx 4$ pm). In **a** and **c**, 0 dB is referenced to 1 mW. **d**, Measured (markers) and simulated (line) conversion efficiency for $i+$ with increasing pump power. **e**, Measured on-chip background noise at $i+$ frequency with ≈ 120 GHz detection bandwidth and the pumps off- and on-resonance with their respective cavity modes. The error bars in **d**-**e** are one standard deviation values caused by fluctuations in the SPAD-detected signal. The 1550 nm pump separation is 1 FSR throughout.

FIG. 5: **Wideband frequency conversion interface to the telecommunications band**. **a**, Schematic for upconversion between the 1550 nm and 980 nm bands. **b**, Representative experimental result for upconversion: the two pumps and signal are located at 974.4 nm, 1564.5 nm and 1528.0 nm, respectively. The small horizontal bar above the signal indicates its input power. In the 980 nm spectrum, along with $i+$ and $i-$, there is a group of small tones near the 980 nm pump due to upconverted EDFA ASE noise, and another small peak near 946.2 nm due to mixing between $i+$ and the 980 nm pump. In the 1550 nm spectrum the small peak near 1602.8 nm is due to mixing of the signal and 1550 nm pump. **c**, Schematic for downconversion between the 980 nm and 1550 nm bands. **d**, Representative experimental result for downconversion showing a full spectrum: the two pumps and signal are located at 974.4 nm, 1559.8 nm, and 961.9 nm, respectively. The small horizontal bar above the signal indicates its input power. In **b** and **d**, a power of 0 dB is referenced to 1 mW.

FIG. 6: **Wideband frequency downconversion bandwidth and background noise measurement. a** Superimposed OSA spectra in the 1550 nm band for different signal separation from the 980 nm pump and fixed pump powers in the 1550 nm and 980 nm bands (50 mW and 8 mW, respectively). The left inset illustrates the signal position and power variation, which contribute to the 1550 nm idler spectra. For both the main figure and its left inset, 0 dB is referenced to 1 mW. The right inset shows the calculated frequency detuning for $i+$ and $i-$ at different idler positions. **b** Measured (markers) and simulated (lines) conversion efficiencies for $i+$ and $i-$ with varying signal separation from the 980 nm pump. **c**-**d**, Measured on-chip background noise power with a 80 GHz detection bandwidth for the pump-off-resonance and resonant noise for $i+$ when the pump is on-resonance for **c**: different idler positions while keeping the 1550 nm pump power fixed at 50 mW and **d**: fixed idler position ($\mu = 7$) while varying the 1550 nm pump power. The one standard deviation error bars in **d** are due to fluctuations in the SPAD detection rate.

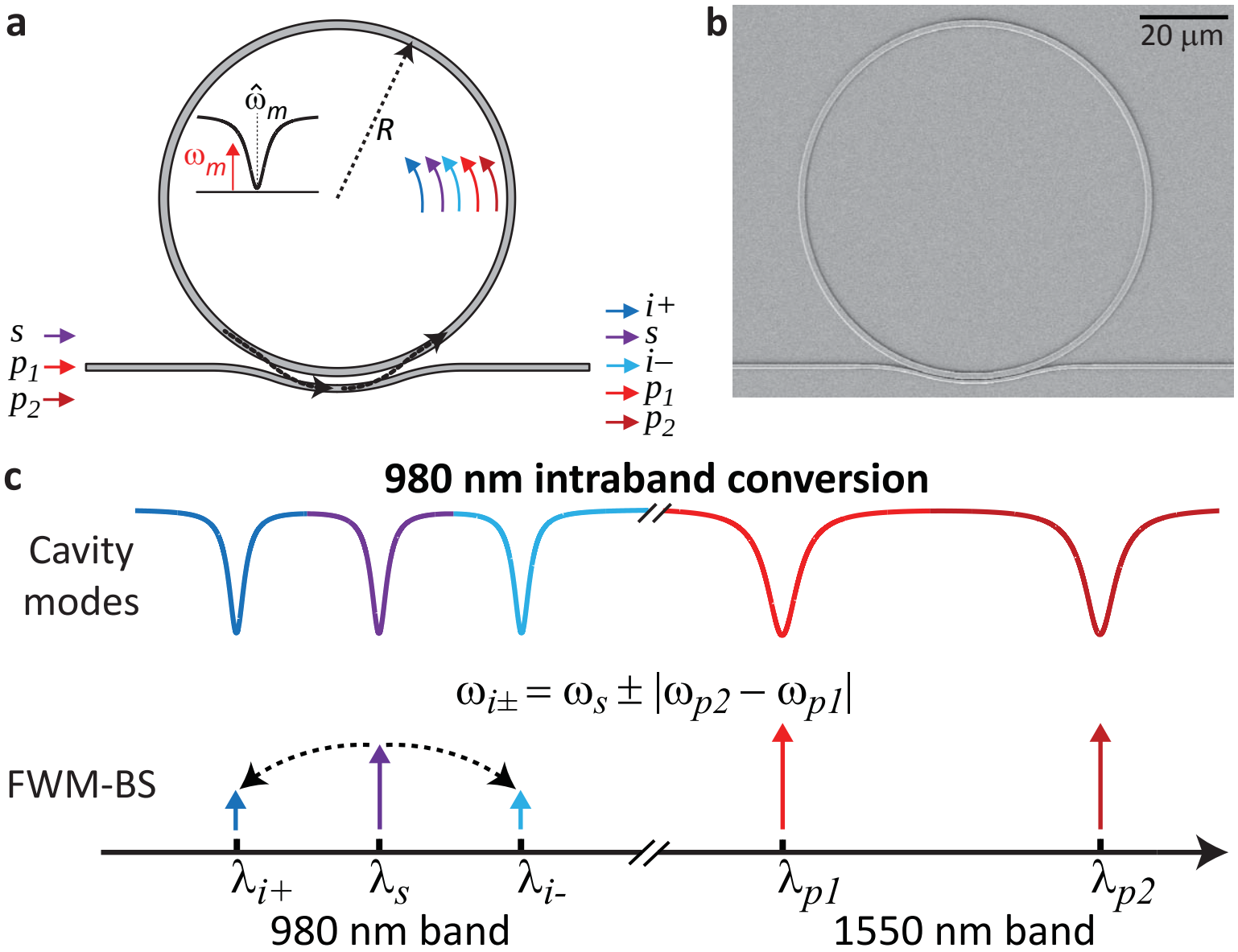
a
$\hat{\omega}_m$
ω_m
R
s
p_1
p_2
$i+$
s
$i-$
p_1
p_2
b
20 μm
c
980 nm intraband conversion
Cavity modes
$\omega_{i\pm} = \omega_s \pm |\omega_{p2} - \omega_{p1}|$
FWM-BS
λ_{i+}
λ_s
λ_{i-}
λ_{p1}
λ_{p2}
980 nm band
1550 nm band

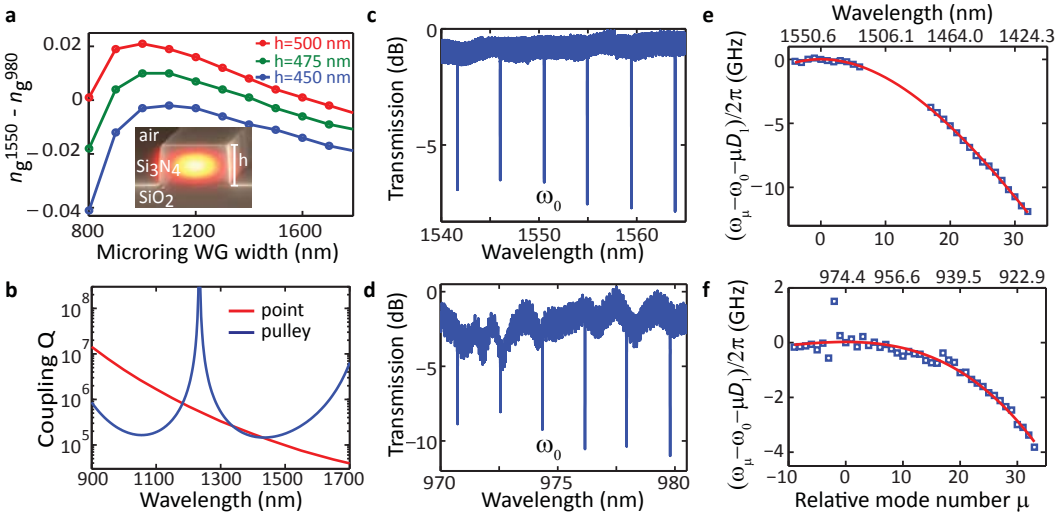
a
h=500 nm
h=475 nm
h=450 nm
air
Si3N4
SiO2
h
Microring WG width (nm)
b
point
pulley
Coupling Q
Wavelength (nm)
c
Transmission (dB)
ω0
Wavelength (nm)
d
Transmission (dB)
ω0
Wavelength (nm)
e
Wavelength (nm)
1550.6 1506.1 1464.0 1424.3
f
974.4 956.6 939.5 922.9
Relative mode number μ

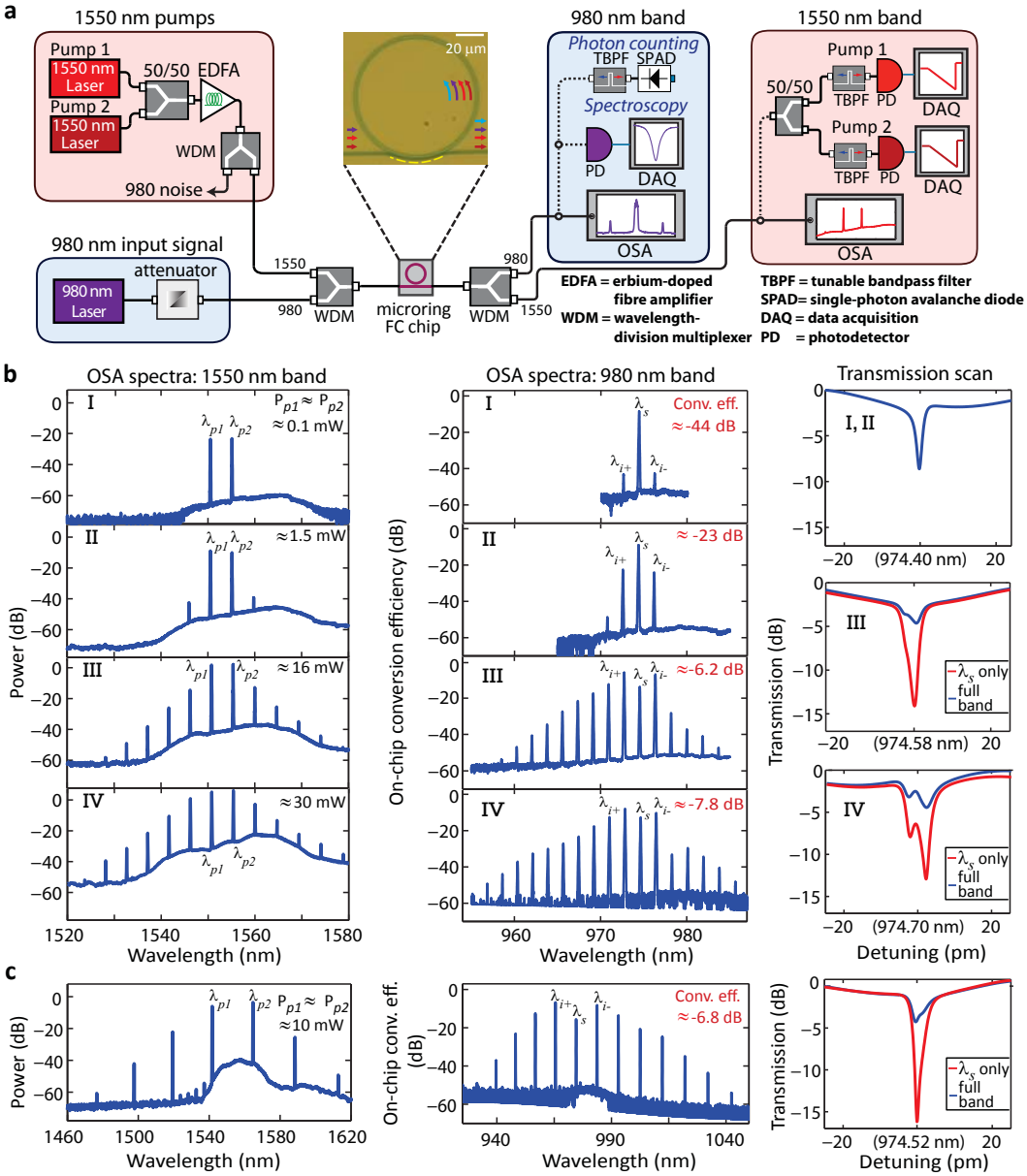
a
1550 nm pumps
Pump 1
1550 nm Laser
Pump 2
1550 nm Laser
50/50
EDFA
WDM
980 noise
980 nm input signal
attenuator
980 nm Laser
1550
980
WDM
20 μm
microring FC chip
980
WDM
1550
980 nm band
Photon counting
TBPF
SPAD
Spectroscopy
PD
DAQ
OSA
1550 nm band
50/50
Pump 1
TBPF
PD
DAQ
Pump 2
TBPF
PD
DAQ
OSA
EDFA = erbium-doped fibre amplifier
WDM = wavelength-division multiplexer
TBPF = tunable bandpass filter
SPAD= single-photon avalanche diode
DAQ = data acquisition
PD = photodetector
b
OSA spectra: 1550 nm band
Power (dB)
Wavelength (nm)
I
II
III
IV
P_p1 ≈ P_p2 ≈0.1 mW
≈1.5 mW
≈16 mW
≈30 mW
OSA spectra: 980 nm band
On-chip conversion efficiency (dB)
Conv. eff. ≈-44 dB
≈ -23 dB
≈-6.2 dB
≈-7.8 dB
Transmission scan
I, II
(974.40 nm)
III
(974.58 nm)
IV
(974.70 nm)
λs only
full band
Transmission (dB)
Detuning (pm)
c
Power (dB)
P_p1 ≈ P_p2 ≈10 mW
Wavelength (nm)
On-chip conv. eff. (dB)
Conv. eff. ≈-6.8 dB
Wavelength (nm)
Transmission (dB)
(974.52 nm)
λs only
full band
Detuning (pm)

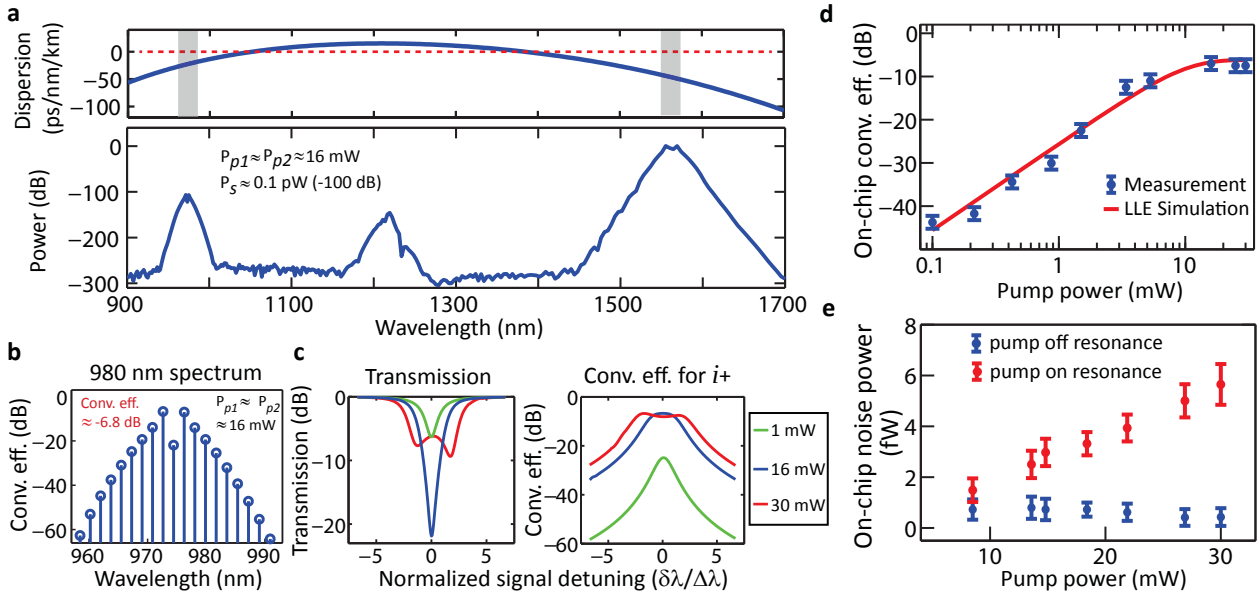
a
Dispersion (ps/nm/km)
0
−50
−100
Power (dB)
0
−100
−200
−300
$P_{p1} \approx P_{p2} \approx 16$ mW
$P_s \approx 0.1$ pW (-100 dB)
900
1100
1300
1500
1700
Wavelength (nm)
b
980 nm spectrum
Conv. eff. ≈ -6.8 dB
$P_{p1} \approx P_{p2} \approx 16$ mW
Conv. eff. (dB)
0
−20
−40
−60
960
970
980
990
Wavelength (nm)
c
Transmission
Transmission (dB)
0
−10
−20
−5
0
5
Conv. eff. for i+
Conv. eff. (dB)
0
−20
−40
−60
1 mW
16 mW
30 mW
Normalized signal detuning (δλ/Δλ)
d
On-chip conv. eff. (dB)
0
−10
−20
−30
−40
0.1
1
10
Measurement
LLE Simulation
Pump power (mW)
e
On-chip noise power (fW)
8
6
4
2
0
pump off resonance
pump on resonance
10
20
30
Pump power (mW)

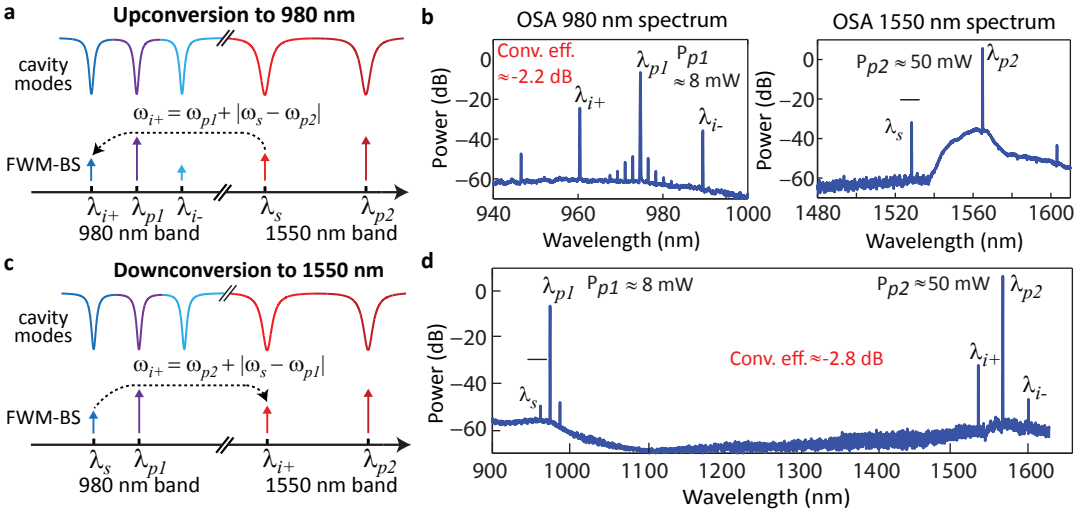
a
Upconversion to 980 nm
cavity modes
$\omega_{i+} = \omega_{p1} + |\omega_s - \omega_{p2}|$
FWM-BS
λ_{i+} λ_{p1} λ_{i-} λ_s λ_{p2}
980 nm band
1550 nm band
b
OSA 980 nm spectrum
Conv. eff. ≈-2.2 dB
λ_{p1} P_{p1} ≈ 8 mW
λ_{i+}
λ_{i-}
Power (dB)
Wavelength (nm)
OSA 1550 nm spectrum
P_{p2} ≈ 50 mW
λ_{p2}
λ_s
c
Downconversion to 1550 nm
cavity modes
$\omega_{i+} = \omega_{p2} + |\omega_s - \omega_{p1}|$
FWM-BS
λ_s λ_{p1} λ_{i+} λ_{p2}
980 nm band
1550 nm band
d
λ_{p1} P_{p1} ≈ 8 mW
P_{p2} ≈ 50 mW
λ_{p2}
Conv. eff. ≈-2.8 dB
λ_{i+}
λ_{i-}
λ_s
Power (dB)
Wavelength (nm)

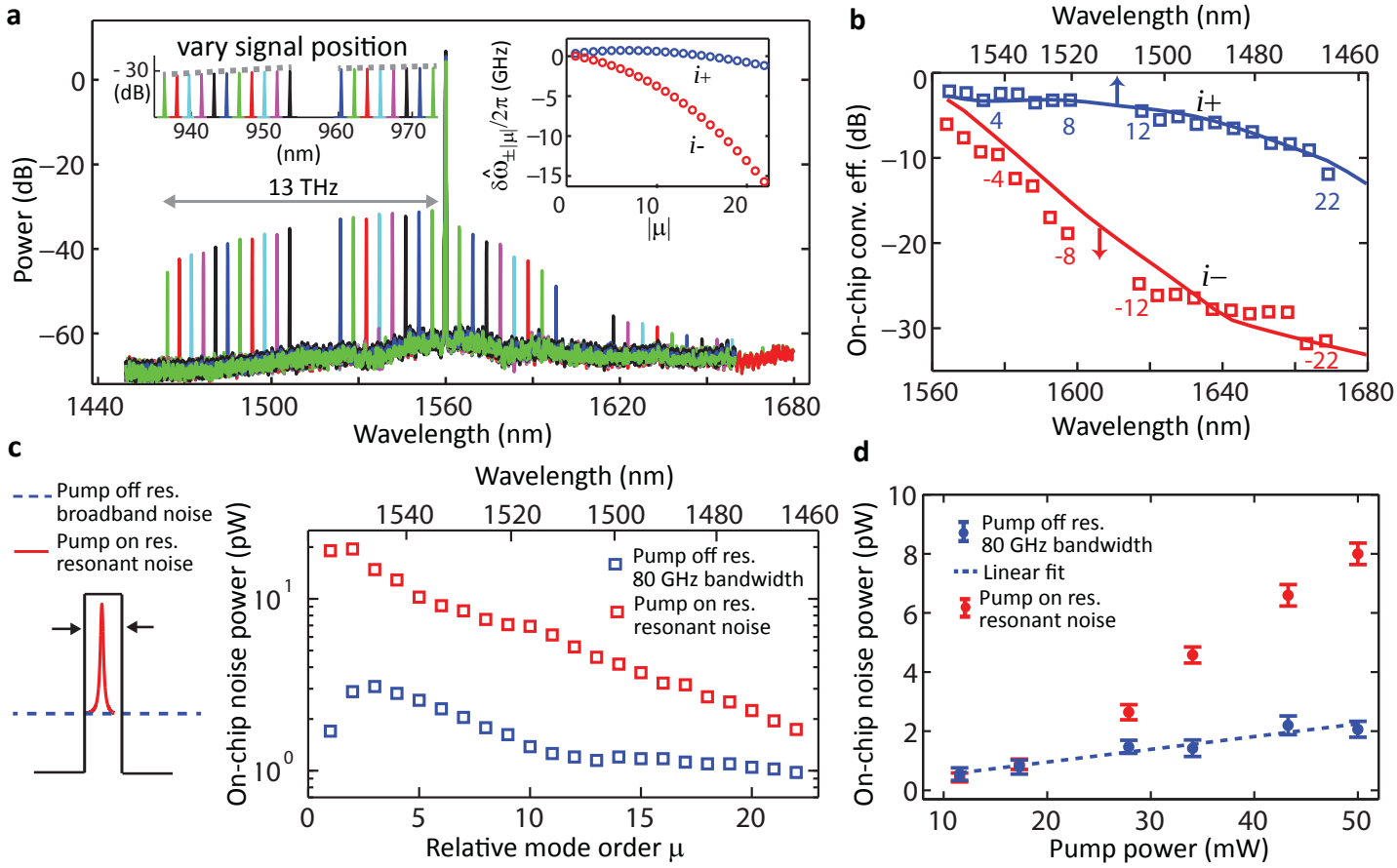
a
vary signal position
- 30 (dB)
940 950 960 970
(nm)
13 THz
Power (dB)
0
−20
−40
−60
1440 1500 1560 1620 1680
Wavelength (nm)
$\delta\hat{\omega}_{\pm|\mu|}/2\pi$ (GHz)
0
−5
−10
−15
i+
i-
0 10 20
|μ|
b
Wavelength (nm)
1540 1520 1500 1480 1460
On-chip conv. eff. (dB)
0
−10
−20
−30
4 8 12 22
-4 -8 -12 -22
i+
i−
1560 1600 1640 1680
Wavelength (nm)
c
Pump off res.
broadband noise
Pump on res.
resonant noise
Wavelength (nm)
1540 1520 1500 1480 1460
On-chip noise power (pW)
10^1
10^0
Pump off res.
80 GHz bandwidth
Pump on res.
resonant noise
0 5 10 15 20
Relative mode order μ
d
On-chip noise power (pW)
10
8
6
4
2
0
Pump off res.
80 GHz bandwidth
Linear fit
Pump on res.
resonant noise
10 20 30 40 50
Pump power (mW)

Supplementary information to Efficient and low-noise single-photon-level frequency conversion interfaces using silicon nanophotonics

Qing Li,[1,2,*] Marcelo Davanço,[1] and Kartik Srinivasan[1,†]

[1] *Center for Nanoscale Science and Technology, National Institute of Standards and Technology, Gaithersburg, MD 20899, USA*
[2] *Maryland NanoCenter, University of Maryland, College Park, MD 20742, USA*

(Dated: February 24, 2016)

This document provides a comparison of our work to previous microresonator-based frequency conversion experiments and some recent four-wave-mixing Bragg scattering experiments. In addition, it contains details on modeling of the four-wave-mixing Bragg scattering process through the Lugiato-Lefever and coupled mode equations. It also provides additional data and discussions from transmission measurements, wideband frequency conversion between the 1550 nm and 980 nm bands, and background noise characterization.

I. COMPARISON WITH FREQUENCY CONVERSION IN MICRORESONATORS BASED ON $\chi^{(3)}$ PARAMETRIC AMPLIFICATION

As discussed in the introduction of the main paper, most previous works on frequency conversion in microresonators have used a degenerate parametric amplification (PA) process. Table S1 compares some representative PA-based frequency conversion experiments to this work (FWM-BS), revealing that our conversion efficiency is significantly higher. We believe the limited efficiencies of those PA-based experiments are due to some technical reasons, which will be discussed below.

To understand how the conversion efficiency for a degenerate PA process scales, we use the expression given by Absil et al (Ref.1), taken in the limit of low conversion efficiency ($\eta \ll 1$) and with the small-signal approximation (SSA):

$$\eta^{\mathrm{PA}} = (\gamma P_p L_{eff})^2 \mathrm{FE}_p^4 \mathrm{FE}_s^2 \mathrm{FE}_i^2, \tag{1}$$

where γ is the Kerr nonlinear coefficient, P_p is the pump power, L_{eff} is the effective propagation length, and FE is the field enhancement factor. While γ is proportional to the material's nonlinear refractive index n_2 (details in Section III.D), FE is determined by the resonator's coupling Q (Q_c) and intrinsic Q (Q_i), as well as the frequency matching condition. For the case that Q_i is high enough and the frequency mismatch is small, L_{eff} is reduced to the resonator circumference L, and FE is given by[1]

$$\mathrm{FE} = \frac{2}{\sigma} \frac{1}{1 + Q_c/Q_i}, \tag{2}$$

where σ is the field coupling coefficient between the ring resonator and the access waveguide ($Q_c = \omega_p t_R/\sigma^2$ with t_R being the roundtrip time).

From Eq. 1, it is obvious that a high FE can reduce the required pump power significantly. On the other hand, for a given resonator, one may tend to think that by increasing the pump power, the conversion efficiency can be improved indefinitely. While there is no fundamental reason that prevents an efficient frequency conversion process based on PA, there are many factors that can limit the achievable conversion efficiency. For instance, since the frequency matching condition is power dependent[2], there is only a certain power range that will provide parametric gain for a fixed signal wavelength. As a result, using a too strong pump will actually reduce the conversion efficiency. On the other hand, if we allow the signal wavelength to be varied to enjoy the maximum parametric gain as the pump power increases, there is still a practical limit on the pump power, that is, it has to be below the parametric oscillation threshold to avoid spontaneous signal/idler generation. Assuming the frequency detuning is kept small, the parametric oscillation threshold is given by[2]

$$\gamma P_{th} L_{eff} \mathrm{FE}_p^2 = \alpha, \tag{3}$$

where α is the total cavity loss ($\alpha = \omega_p t_R/(2Q_L)$). Substituting this into Eq. 1, a crude estimate on the maximum achievable conversion efficiency for a PA-based process can be obtained as

$$\eta_{\mathrm{max}}^{\mathrm{PA}} = \left(\frac{2}{1 + Q_c/Q_i} \right)^2, \tag{4}$$

which indicates that if the resonator is severely undercoupled ($Q_c \gg Q_i$), the maximum achievable conversion efficiency is much less 100%, even if the resonator has very high Q_i. Therefore, to achieve an efficient conversion process, it is important to design the coupling of the resonator to be in the overcoupled regime, a key point emphasized by this work. Finally, the amount of

pump power that can be injected into the resonator can be further restricted by the material's properties. In silicon, for example, two photon absorption (TPA) and TPA-induced free carriers generate significant nonlinear loss when the pump power is high enough, in which case the frequency conversion becomes less efficient as FE drops more quickly (Q_i decreases) than the benefit provided by the increase of the pump power.

As a comparison, here we also provide a brief qualitative discussion on the FWM-BS process. Similar to the degenerate PA, for small η the conversion efficiency of a frequency-matched FWM-BS can be obtained from the SSA as

$$\eta^{\mathrm{BS}} = (2\gamma P_p L_{eff})^2 \mathrm{FE}_p^4 \mathrm{FE}_s^2 \mathrm{FE}_i^2, \tag{5}$$

where the additional factor of 2 in the parenthesis is due to the use of two non-degenerate pumps (Note that for η close to 1 it is important to use a more complete model to calculate the conversion efficiency, which we present in Section III). Unlike PA which has parametric gain, in the FWM-BS process the photon number is conserved. In addition, even if the signal can be fully converted to the idler inside the microresonator, only a fraction of the idler is coupled to the waveguide while the rest is dissipated during propagation within the ring. Using this simple argument, one concludes that the maximum conversion efficiency for FWM-BS is given by

$$\eta_{\mathrm{max}}^{\mathrm{BS}} = \frac{1}{1+Q_c/Q_i}. \tag{6}$$

Thus, it is important to minimize the propagation loss to ensure that the resonator is in the overcoupled regime. In principle, by decreasing the Q_c/Q_i ratio, the conversion efficiency can approach the maximum possible value, i.e., 100%.

TABLE S1: Comparison of frequency conversion experiments using microrings

Material platform	Refractive index	n_2 ($\mathrm{m^2W^{-1}}$)	Representative experiment	γ @1550 nm ($\mathrm{m^{-1}W^{-1}}$)	Radius (μm)	Q_L @1550 nm ($\times 10^3$)	FE	Peak pump power (mW)	On-chip CE (dB) Theory	Experiment
AlGaAs	3.3	1.3×10^{-17}	P. P. Absil, et al. [1]	105	7	≈ 3	2.1	140	-38.8	-44.6
Hydex	1.7	1.15×10^{-19}	M. Ferrera et al. [3]	0.233	48	65	-	19	-	-49
			M. Ferrera et al. [4]	0.233	135	1200	17.9	8.8	-15	-26
Si	3.45	(3-6.5)$\times10^{-18}$	A. C. Turner et al. [5]	-	50	19	-	11.3	-	-25.4
			J. R. Ong et al. [6]	190	20	50	-	2.5	-	-13.4
Si_3N_4	2.0	2.5×10^{-19}	This work	2.07	40	150	14.1	58	-1.8	-2.2

II. COMPARISON WITH OTHER FWM-BS EXPERIMENTS AND ROUTES TO IMPROVING DEVICE PERFORMANCE

In table S2, we compare our current results with other recent FWM-BS measurements in photonic crystal fiber (PCF), highly nonlinear fiber (HNLF), and Si_3N_4 waveguides. Our current work is distinguished by achieving high conversion efficiency and good SNR for single-photon-level inputs using continuous wave (CW) pumps with modest power levels (tens of mW), all in a compact, chip-scale geometry. Moreover, we have demonstrated that the same geometry can be used for both intraband conversion across a few nm and wideband conversion across hundreds of nm.

On the other hand, this performance is partly achieved through the use of a resonant geometry, which imposes constraints on the tunability of the spectral translation range, the need to match the resonant wavelengths to the input signal and available pump sources, and the bandwidth of the signals that can be converted. In the remainder of this section, we discuss some of the tradeoffs involved in using a resonant geometry, and more generally, consider what future steps may be taken to improve the device performance.

We start with the discussion on the conversion efficiency, which is the single most important metric for a frequency converter. For the current device, the maximum conversion efficiency of the 980 nm intraband conversion is around 25% for each of the first-order idlers. It is obvious that the conversion efficiency will be limited to 50% if the incoming signal photons are equally converted to the blue and red idlers. Therefore, one straightforward way to improve the efficiency is to design the resonator dispersion such that only the blue or red idler is frequency matched while the other one is suppressed, similar to the wideband conversion case as shown in Figs. 5 and 6 in the main paper. This can be achieved by increasing the spectral separation between the two pumps in the 1550 nm band as well as the dispersion in the 980 nm band. (Note that D_2 of the current device in the 980 nm band is almost 10 times smaller than that of the 1550 nm band.) The increase of the pump separation also reduces the pump mixing effect, resulting in fewer high-order idlers and consequently higher conversion efficiency. For the wideband frequency conversion between the 1550 nm and 980 nm bands, the conversion efficiency is limited to around 60% for the device under test. As discussed in the previous section (Eq. 6), one clear route to improving the efficiency is to reduce the Q_c/Q_i ratio. This work

TABLE S2: Comparison of recent four-wave-mixing Bragg scattering frequency conversion experiments

Medium	$\lambda_i - \lambda_s$ (nm)	Pump Type	Total Peak Pump Power $P_{p1} + P_{p2}$ (mW)	Conversion Efficiency (dB)	SNR for single-photon-level input signal	Notes	Reference
32 m PCF	-24	Pulsed	6600	-5.4	See Note	*a*	McGuinness et al. [7]
10 m PCF	-210	Pulsed and CW	12000	-27	N/A	*b*	McGuinness et al. [8]
9 cm Rb-filled PCF	-14	CW	0.6	-6.8	N/A	–	Donvalkar et al. [9]
750 m HNLF	12	CW	300	-0.04	N/A	*c*	Clark et al. [10]
12 mm Si_3N_4 WG	3	Pulsed	14000	-13	N/A	–	Agha et al. [11]
18 mm Si_3N_4 WG	575	CW	56	-64	See Note	*d*	Agha et al. [12]
80 μm diameter Si_3N_4 ring	1.8-9.0	CW	32	-6.2	80 : 1	*e*	This work
80 μm diameter Si_3N_4 ring	580	CW	58	-2.2	$> 1 : 1$	*f*	This work

[a] In this work, a true heralded single photon source was used to demonstrate quantum frequency conversion, with $g^{(2)}(0) = 0.21 \pm 0.02$ before frequency conversion and $g^{(2)}(0) = 0.19 \pm 0.05$ after frequency conversion, indicating that the SNR should be good. However, no quantification of the SNR using our approach (measuring the photon flux in the idler conversion band with and without a single-photon-level input signal) was performed.

[c] Conversion efficiency defined in terms of signal depletion rather than idler generation (thought to be unequal due to Raman depletion). Detailed SNR measurements were not presented but the text qualitatively notes a noise power that is comparable to the signal power.

[d] While SNR levels of 10 : 1 are reported in the paper, the very low conversion efficiency required an input signal level $> 10^{10}$ photons/s, well in excess of the 5×10^6 photons/s used in the current work. Therefore, a direct comparison is difficult to make.

[e] Use of resonant geometry limits spectral translation range to discrete values (set by 980 nm band FSR $\approx$1.8 nm) and signal bandwidth to ≈ 1.3 GHz (set by the cavity Q).

[f] Use of resonant geometry limits spectral translation range to discrete values (set by 980 nm band FSR $\approx$1.8 nm and 1550 nm band FSR ≈ 4.6 nm) and signal bandwidth to ≈ 1.3 GHz (set by the cavity Q).

uses a microring with an intrinsic Q around 4.5×10^5 in the 1550 nm band (9×10^5 in the 980 nm band), which can be improved to a few million with a more optimized fabrication process[13]. While a higher intrinsic Q is always preferred, the loaded Q is determined by the targeted application. For example, our approximately 1 GHz resonance linewidth is motivated by the emission bandwidth of InAs/GaAs quantum dots, which is typically around a few hundred MHz. This translates to a loaded Q around 2×10^5 in the 1550 nm band. Figure S1a shows the simulation results for conversion efficiency as a function of intrinsic Q, for a frequency-matched downconversion process studied using the coupled mode theory formalism of Section III.B. With a fixed coupling Q of 2×10^5 and a total pump power of 58 mW, the conversion efficiency reaches $> 85\%$ if the intrinsic Q is larger than 2×10^6, a practically achievable number. We note that the simple expression from Eq. 6 gives $\eta = 91\%$, with the degradation of efficiency from the coupled mode simulations due to the slight frequency mismatch induced by the Kerr phase shift at high power.

Next, we provide a brief discussion on the tradeoff between the device size and other performance metrics such as pump power requirement. In this work, a compact microresonator with radius of 40 μm is used to achieve a small footprint ($< 0.5 \times 10^{-4}$ cm^2). However, the FSR of our ring stands around 570 GHz, which makes the bandwidth usage inefficient (approximately 1 GHz out of 570 GHz). More importantly, considering the limited fabrication resolution (≈ 5 nm), it is difficult to match the resonance wavelength to the emission wavelength of a specific quantum dot, so a resonance frequency tuning mechanism (either in-situ or post-fabrication trimming) is required[14]. In practice, a smaller FSR (thus a larger ring) makes the frequency matching between the resonator and quantum dots less challenging. On the other hand, since we want to keep the loaded Q fixed ($\approx 2 \times 10^5$) from the bandwidth matching consideration, there is less resonance enhancement as we increase the resonator size, resulting in a higher pump power requirement. Figure S1b shows that while the FSR is inversely proportional to the ring radius, the required pump power has to linearly increase to keep a constant conversion efficiency. Unfortunately, such tradeoff between the resonator size (FSR) and pump power is quite inherent to a resonator-based device, and hence a careful choice of the ring radius has to be made depending on specific circumstances.

Our focus in this work has been on compatibility with quantum dot single photon sources, and as we have mentioned above and in the main paper, the > 1 GHz bandwidth (e.g., Fig. 4c in the main paper) is compatible with such sources. We also expect, based on the ability to tailor the FWM-BS process, to be able to extend our work to connect other single quantum emitters with the telecom band, which would be an important general resource in the application of these systems for photonic quantum information science. This includes NV centers in diamond (637 nm), Rb atoms (780 nm), and Cs atoms (852 nm), all of which have emission bandwidths < 1 GHz. Moreover, such systems have extremely small inhomogeneous broadening compared to InAs/GaAs quantum dots, so that the emission wavelength is essentially known a priori and post-fabrication trimming methods (e.g., dilute HF etching of Si_3N_4 or atomic layer deposition of a thin cladding layer) can be used to achieve cavity resonances

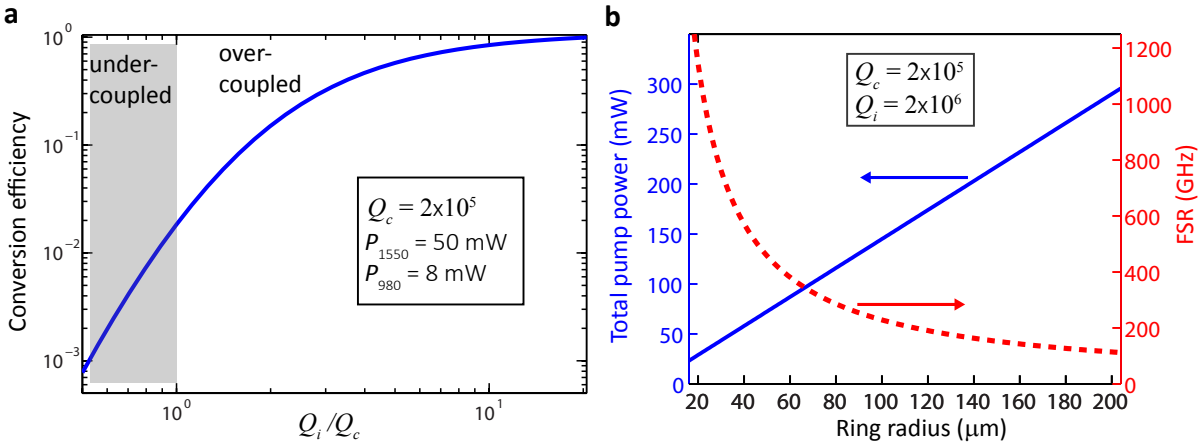

FIG. S1: **a**, Conversion efficiency of a frequency-matched downconversion process as a function of resonator's intrinsic Q with its coupling Q fixed at 2×10^5 in the 1550 nm band. The pump power is also fixed at 50 mW and 8 mW for the 1550 nm band and 980 nm band pump, respectively. **b**, Scaling of the required pump power (left axis) and FSR (right axis) versus the ring radius for 85% conversion efficiency. The coupling (intrinsic) Q is assumed to be 2×10^5 (2×10^6) in the 1550 nm band. The power ratio between the 1550 nm pump and 980 pump is assumed to be fixed at 50 to 8.

at the desired target wavelengths. One other point in considering the tradeoff between waveguide and resonator frequency conversion geometries is that the use of short pulsed pumps to improve the conversion efficiency in some waveguide works (e.g., Refs.7,8,11) can also present a restriction for some quantum frequency conversion experiments, when the pump pulse duration is significantly shorter than the single photon wavepacket duration. This can be true for many single quantum emitter systems, whose photonic wavepacket duration is in the ns to μs regime. For such systems, high conversion efficiencies most likely need to be achieved under continuous wave pumping.

Finally, we want to say a few words about the thermal properties of the Si_3N_4 resonator. The thermal issue mainly arises from the heating of the resonator due to material absorption. The annealing of Si_3N_4 is expected to make the material transparent, though in our case it seems there is still a significant amount of absorption remaining. This has caused several issues. First, a dual-pump thermal locking has to be performed, which is an iterative procedure to tune both pumps into their respective thermally-shifted resonances. Though this procedure requires some additional effort in the experiment, it is actually quite straightforward and can in principle be automated. Second, the heat generated in each resonator can diffuse to adjacent areas, which is a potential problem if such resonator-based frequency converters are densely integrated on chip. While this concern is valid to some degree, there are well-developed techniques such as thermal trenches to eliminate the thermal cross talk between devices[15]. In addition, advanced designs such as athermal resonators may also help combat the thermal issue[16]. Lastly, we believe the relatively large noise observed in the 1550 nm band from a strong 1550 nm pump (Fig. 6c) is also related to the imperfect Si_3N_4 material property (see detailed discussions in Section VIII), and expect a reduced noise power if better Si_3N_4 can be grown or a more effective annealing process can be developed.

III. FWM-BS: THEORY AND NUMERICAL SIMULATIONS

The conventional LLE formalism describes the Kerr nonlinearity in a $\chi^{(3)}$ microring resonator as [17,18]

$$t_R\frac{\partial E(t,\tau)}{\partial t}=\left[-\alpha-i\delta_0+iL\sum_{k\geq2}\frac{\beta_k}{k!}\left(i\frac{\partial}{\partial\tau}\right)^k+i\gamma L|E(t,\tau)|^2\right]E(t,\tau)+i\sqrt{\theta}E_{\rm in}, \tag{7}$$

where t_R is the round-trip time, $E(t,\tau)$ is the intracavity mean field with $|E(t,\tau)|^2$ representing the average power traveling inside the cavity (τ is the time and t is a parameter measuring the slow time of the cavity), α and δ_0 are the total cavity loss and detuning at the resonance frequency $\hat{\omega}_0$, respectively ($\alpha=\hat{\omega}_0 t_R/(2Q_L)$ with Q_L being the loaded Q and $\delta_0=(\hat{\omega}_0-\omega_0)t_R$ with ω_0 being the frequency of the driving field), L is the round-trip length of the resonator, $\beta_k(k\geq2)$ are the second and higher-order dispersion parameters of the ring waveguide, γ is the Kerr nonlinear coefficient, θ is the power coupling coefficient between the resonator and the access waveguide or fiber ($\theta=\hat{\omega}_0 t_R/Q_c$ with Q_c being the coupling Q), and $E_{\rm in}$ is a continuous-wave driving field (input power $P_{\rm in}=|E_{\rm in}|^2$). Figure S2 schematically depicts the system under investigation, and includes a table of the aforementioned variables.

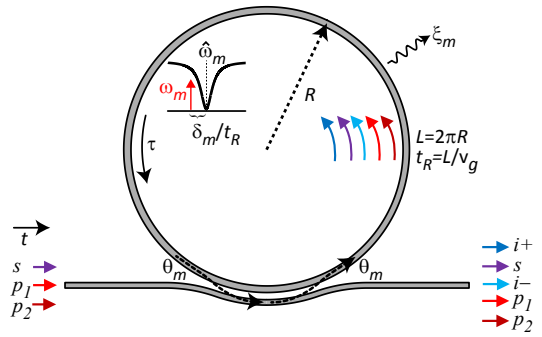

Variable name	Description	Equation
s	input signal	-
$p1$	pump 1	-
$p2$	pump 2	-
$i+$	blue-shifted idler	-
$i-$	red-shifted idler	-
τ	time	-
t	slow time scale set by cavity	-
t_R	cavity round-trip time	-
L	cavity round-trip length	-
ω_m	frequency of driving field near mode m	-
$\hat{\omega}_m$	frequency of mode m	-
E_m	intracavity electric field for mode m	-
E_{in,ω_m}	driving field at frequency ω_m	-
$Q_{i,m}$	intrinsic Q for mode m	-
$Q_{c,m}$	coupling Q for mode m	-
$Q_{L,m}$	total loaded Q for mode m	$Q_{L,m}^{-1}=Q_{i,m}^{-1}+Q_{c,m}^{-1}$
α_m	cavity mode m total loss rate	$\hat{\omega}_m t_R/(2Q_{L,m})$
ξ_m	intrinsic loss rate for mode m	$\hat{\omega}_m t_R/Q_{i,m}$
θ_m	waveguide power coupling rate for mode m	$\hat{\omega}_m t_R/Q_{c,m}$
δ_m	laser-cavity mode m detuning	$\delta_m=(\hat{\omega}_m-\omega_m)t_R$
γ_m	nonlinear coefficient for mode m	see Section I.D

FIG. S2: (Left) Schematic and (Right) table listing the parameters used in the LLE and coupled mode equations models of the four-wave-mixing Bragg scattering process.

As mentioned in the main paper, the LLE formalism is equivalent to coupled mode equations [19,20]. In fact, $E(t,\tau)$ can be viewed as a collection of resonant modes $\{E_m(t)\}$ (m is the azimuthal order) oscillating on an equally spaced frequency grid $\{\omega_m\}$ ($E(t,\tau)=\sum_m E_m(t)\exp(-i\omega_m\tau)$), whose governing coupled mode equation can be obtained through a Fourier transform of Eq. 7. However, for the FWM-BS process we have three driving fields (instead of only one pump in the standard LLE formalism), and each can have its own detuning with respect to the nearest cavity mode. Thus, the coupled mode equations should present the following form:

$$t_R\frac{dE_m}{dt}=-(\alpha_m+i\delta_m)E_m+i\gamma_m L\mathcal{F}\left\{|E(t,\tau)|^2E(t,\tau)\right\}_m+i\sqrt{\theta_m}E_{\mathrm{in},m}, \tag{8}$$

where $\mathcal{F}$ stands for the Fourier transform, and all the parameters and expressions with subscript m are meant to be computed at frequency ω_m. In particular, the detuning parameter δ_m is given by $\delta_m=(\hat{\omega}_m-\omega_m)t_R$, where the resonance frequency $\hat{\omega}_m$ is determined by a self-consistent equation $\hat{\omega}_m=\hat{\omega}_0+\sum_{k\geq 1}L\beta_k(\hat{\omega}_m-\hat{\omega}_0)^k/(k!t_R)$. In the experiment, the frequencies of the driving fields for the two pumps and the signal ($\omega_{p1,p2,s}$) are free parameters that can be varied to achieve an optimum frequency conversion efficiency. On the other hand, the frequency of the generated idlers ($\omega_{i\pm}$) is determined by the energy conservation condition, and therefore is a function of $\omega_{p1,p2,s}$ (see Fig. 1c for the 980 nm intraband conversion and Fig. 5 for wideband conversion in the main paper).

In the following, we will discuss the detailed implementations of coupled mode equations as well as a modified LLE method for the FWM-BS process.

A. Coupled mode equations for 980 nm intraband conversion

We start with a simplified set of coupled mode equations for the intraband frequency conversion in the 980 nm band, that is, we neglect pump mixing in the 1550 nm band and high-order idlers in the 980 nm band. As a result, the modes under consideration are: two pumps ($p1$ and $p2$), the signal (s), and two idlers ($i+$ and $i-$). Following Eq. 8, the coupled mode equation for pump 1 can be written as

$$t_R\frac{dE_{p1}}{dt}=-(\alpha_{p1}+i\Delta\phi_{p1})E_{p1}+i\sqrt{\theta_{p1}P_{p1}}, \tag{9}$$

where we have combined δ_{p1} and the Kerr nonlinear shift into an effective detuning $\Delta\phi_{p1}$, which is given by

$$\Delta\phi_{p1} = (\hat{\omega}_{p1} - \omega_{p1})t_R - \gamma_{p1}L(|E_{p1}|^2 + 2|E_{p2}|^2). \tag{10}$$

For a steady state, Eq. 9 gives $E_{p1} = i\sqrt{\theta_{p1}P_{p1}}/(\alpha_{p1} + i\Delta\phi_{p1})$. Similarly, for pump 2 we obtain $E_{p2} = i\sqrt{\theta_{p2}P_{p2}}/(\alpha_{p2} + i\Delta\phi_{p2})$ and its effective detuning $\Delta\phi_{p2}$ as

$$\Delta\phi_{p2} = (\hat{\omega}_{p2} - \omega_{p2})t_R - \gamma_{p2}L(2|E_{p1}|^2 + |E_{p2}|^2). \tag{11}$$

Next, we derive the coupled mode equations for the signal and idlers as

$$t_R\frac{dE_s}{dt} = -(\alpha_s + i\Delta\phi_s)E_s + i2\gamma_s L E_{p1}E_{p2}^* E_{i-} + i2\gamma_s L E_{p1}^* E_{p2}E_{i+} + i\sqrt{\theta_s P_s}, \tag{12}$$

$$t_R\frac{dE_{i+}}{dt} = -(\alpha_{i+} + i\Delta\phi_{i+})E_{i+} + i2\gamma_{i+}LE_{p1}E_{p2}^* E_s, \tag{13}$$

$$t_R\frac{dE_{i-}}{dt} = -(\alpha_{i-} + i\Delta\phi_{i-})E_{i-} + i2\gamma_{i-}LE_{p1}^* E_{p2}E_s, \tag{14}$$

with their effective detunings given by

$$\Delta\phi_s = (\hat{\omega}_s - \omega_s)t_R - 2\gamma_s L(|E_{p1}|^2 + |E_{p2}|^2), \tag{15}$$

$$\Delta\phi_{i+} = (\hat{\omega}_{i+} - \omega_{i+})t_R - 2\gamma_{i+}L(|E_{p1}|^2 + |E_{p2}|^2), \tag{16}$$

$$\Delta\phi_{i-} = (\hat{\omega}_{i-} - \omega_{i-})t_R - 2\gamma_{i-}L(|E_{p1}|^2 + |E_{p2}|^2). \tag{17}$$

Because of energy conservation, $\omega_{i\pm} = \omega_s \pm |\omega_{p1} - \omega_{p2}|$. Using Eqs. 10, 11, and 15, we can express the detunings of the two idlers as

$$\Delta\phi_{i+} = (\hat{\omega}_{i+} - \hat{\omega}_s - |\hat{\omega}_{p1} - \hat{\omega}_{p2}|)t_R + \Delta\phi_s + (\Delta\phi_{p1} - \Delta\phi_{p2}) - \gamma^{1550}L(|E_{p1}|^2 - |E_{p2}|^2), \tag{18}$$

$$\Delta\phi_{i-} = (\hat{\omega}_{i-} - \hat{\omega}_s + |\hat{\omega}_{p1} - \hat{\omega}_{p2}|)t_R + \Delta\phi_s - (\Delta\phi_{p1} - \Delta\phi_{p2}) + \gamma^{1550}L(|E_{p1}|^2 - |E_{p2}|^2), \tag{19}$$

where we have used the approximation $\gamma_s \approx \gamma_{i+} \approx \gamma_{i-} \approx \gamma^{980}$, since the signal and idlers are close in wavelength. Likewise, for the two pumps, $\gamma_{p1} \approx \gamma_{p2} \approx \gamma^{1550}$. It it worth noting that the frequency detuning $\delta\hat{\omega}_\pm$ defined in the main paper is proportional to the first part of $\Delta\phi_{i\pm}$, as in our experiment (Fig. 3 in the main paper) the two pumps are operated under similar conditions ($P_{p1} \approx P_{p2}$ and $\Delta\phi_{p1} \approx \Delta\phi_{p2}$) and the signal is typically set at the minimum of its transmission ($\Delta\phi_s \approx 0$), thus making the first part the dominant term.

TABLE S3: Additional variables used in the coupled mode equations

Variable name	Description	Equation
$\Delta\phi_{p1}$	Effective detuning for pump 1	Eq. 10
$\Delta\phi_{p2}$	Effective detuning for pump 2	Eq. 11
$\Delta\phi_s$	Effective detuning for the input signal	Eq. 15
$\Delta\phi_{i+}$	Effective detuning for the blue-shifted idler	Eqs. 16 and 18
$\Delta\phi_{i-}$	Effective detuning for the red-shifted idler	Eqs. 17 and 19
Ω_0	Effective nonlinear parameter	$\Omega_0 = 2\gamma^{980}L\lvert E_{p1}E_{p2}\rvert$
Ω_1	Asymmetry in idler detuning	$(\Delta\phi_{i+} - \Delta\phi_{i-})/2$
Ω_2	Mean idler detuning	$(\Delta\phi_{i+} + \Delta\phi_{i-})/2$

The coupled mode equations (Eqs. 12-14) generally have three eigenmodes with different eigenfrequencies, readily suggesting mode splitting in the transmission. To gain some insight, we carry out a brief analytical study here. First, we define three parameters: $\Omega_0 \equiv 2\gamma^{980}L|E_{p1}E_{p2}|$, $\Omega_1 \equiv (\Delta\phi_{i+} - \Delta\phi_{i-})/2$, and $\Omega_2 \equiv (\Delta\phi_{i+} + \Delta\phi_{i-})/2$. Using the result of $\delta\hat{\omega}_\pm$ obtained in the main paper (i.e., $\delta\hat{\omega}_{\pm|\mu|} \approx \pm\delta D_1|\mu| + \frac{1}{2}\delta D_{2,\mp}\mu^2$, where μ stands for the azimuthal order difference between the two pumps), we arrive at

$$\Omega_1 \approx \delta D_1|\mu|t_R - \frac{1}{2}D_2^{1550}\mu^2 t_R + \Delta\phi_{p1} - \Delta\phi_{p2} - \gamma^{1550}L(|E_{p1}|^2 - |E_{p2}|^2), \tag{20}$$

$$\Omega_2 \approx \frac{1}{2}D_2^{980}\mu^2 t_R. \tag{21}$$

One can easily identify the factors affecting Ω_1 are: the FSR mismatch between the 1550 nm and 980 nm bands, the second order dispersion in the 1550 nm band, and the experimental operating conditions of the two 1550 nm pumps (especially the symmetry). Ω_2, on the other hand, is generally small and purely determined by the dispersion of the 980 nm band (in particular, it is independent of the two pump settings). Here we approximate $\Omega_2 \approx 0$, and the three eigenfrequencies can be calculated as

$$\hat{\omega}_{e1} \approx \hat{\omega}_s, \tag{22}$$

$$\hat{\omega}_{e2} \approx \hat{\omega}_s + \frac{1}{t_R}\sqrt{2\Omega_0^2 + \Omega_1^2}, \tag{23}$$

$$\hat{\omega}_{e3} \approx \hat{\omega}_s - \frac{1}{t_R}\sqrt{2\Omega_0^2 + \Omega_1^2}. \tag{24}$$

It is also interesting to find the corresponding eigenmodes, which are

$$|\mathbf{e}_1\rangle = N_1\left(\frac{1}{\sqrt{1+2\eta^2}}|\mathbf{s}\rangle - \frac{\eta}{\sqrt{1+2\eta^2}}|\mathbf{i}+\rangle + \frac{\eta}{\sqrt{1+2\eta^2}}|\mathbf{i}-\rangle\right), \tag{25}$$

$$|\mathbf{e}_2\rangle = N_2\left(|\mathbf{s}\rangle + \frac{\eta}{\sqrt{1+2\eta^2}-1}|\mathbf{i}+\rangle + \frac{\eta}{\sqrt{1+2\eta^2}+1}|\mathbf{i}-\rangle\right), \tag{26}$$

$$|\mathbf{e}_3\rangle = N_3\left(|\mathbf{s}\rangle - \frac{\eta}{\sqrt{1+2\eta^2}+1}|\mathbf{i}+\rangle - \frac{\eta}{\sqrt{1+2\eta^2}-1}|\mathbf{i}-\rangle\right), \tag{27}$$

where $\eta \equiv \Omega_0/\Omega_1$ and N_k is a normalization factor for $|\mathbf{e}_k\rangle$ to ensure $\langle \mathbf{e}_k|\mathbf{e}_k\rangle = 1$ ($k = 1,2,3$). Generally, the state of photons travelling inside the cavity will be a superposition of these three eigenmodes, with the coefficients determined by parameters including α_s (cavity linewidth) and $[\Omega_0\ \Omega_1\ \Omega_2]$. Down to single photon level, the square of the coefficient associated with each eigenmode can be interpreted as the probability of finding the injected photon in this particular mode.

Next, numerical simulations are carried out in Fig. S3 to investigate the effect of different combinations of $[\Omega_0\ \Omega_1\ \Omega_2]$ to the frequency conversion process (the two pumps are assumed to have equal power and detuning). Figure S3a plots the reference example, which corresponds to the device under study for a pump power of 30 mW per pump. The transmission scan of the signal resonance (left figure) and the conversion efficiency for the blue and red idlers (right figure) as a function of signal detuning are similar to the experimental results (Fig. 3b, case IV) and the LLE simulation (Fig. 4c) shown in the main paper. The asymmetric mode splitting observed in the transmission scan is due to a nonzero Ω_2, which is negative for our device (see Eq. 21 and note $D_2^{980} < 0$ since the resonator shows normal dispersion in both 1550 nm and 980 nm bands). If Ω_2 is positive, as illustrated by Fig. S3b, the asymmetry in the transmission scan is mirrored in the spectrum, whereas a symmetric mode splitting is expected if Ω_2 is zero.

Figures S3c-d explore how the pump power affects the frequency conversion process (varying Ω_0), which shows that the maximum conversion efficiency for both blue and red idlers is limited to ≈ -5 dB for pump powers larger than 16 mW. In addition, as the pump power increases, the mode splitting becomes stronger and the optimum signal detuning corresponding to the maximum conversion efficiency for the blue and red idlers shifts away from origin. Therefore, if we choose to use a fixed signal detuning (such as zero), the conversion efficiency will start to decrease with the pump power after reaching its optimum value[21]. Finally, Figs. S3e-f study the effect of Ω_1, that is, the asymmetry in the idler detunings with respect to the nearest cavity modes. According to Eq. 20, its absolute value can be easily comparable to the cavity loss rate if the separation between the two 1550 nm pumps ($|\mu|$) or the FSR mismatch between the 1550 nm and 980 nm bands is large enough. In addition, its value can change significantly if the two pumps are operated under different conditions (such as $P_{p2} \gg P_{p1}$ as in the wideband conversion experiment shown in the main paper). The simulation shows that as $|\Omega_1|$ increases (Fig. S3e), we start to see three dips in the transmission scan, corresponding to the three eigenmodes of the coupled system (a similar spectrum has been observed in the experiment for a different device, though the data not is shown here). Moreover, unlike the previous examples (Figs. S3a-d) where the blue and red idlers show similar conversion efficiencies, in this case only one idler can reach its maximum conversion efficiency while the other one is much weaker. Further increasing $|\Omega_1|$ (Fig. S3f) results in a bigger contrast between the blue and red idlers if one of them is set at its optimum conversion efficiency. However, if $|\Omega_1|$ is too large ($> 5\alpha_s$ for the pump power of 30 mW), the maximum achievable conversion efficiency for both idlers drops significantly (< 10 %), and the transmission scan of the signal resonance starts to look like the linear case.

B. Coupled mode equations for wideband frequency conversion

The coupled mode equations for the wideband frequency conversion can be derived following a similar fashion as in the previous subsection. Especially, as demonstrated by Fig. 5d in the main paper, the pump mixing is absent in the wideband

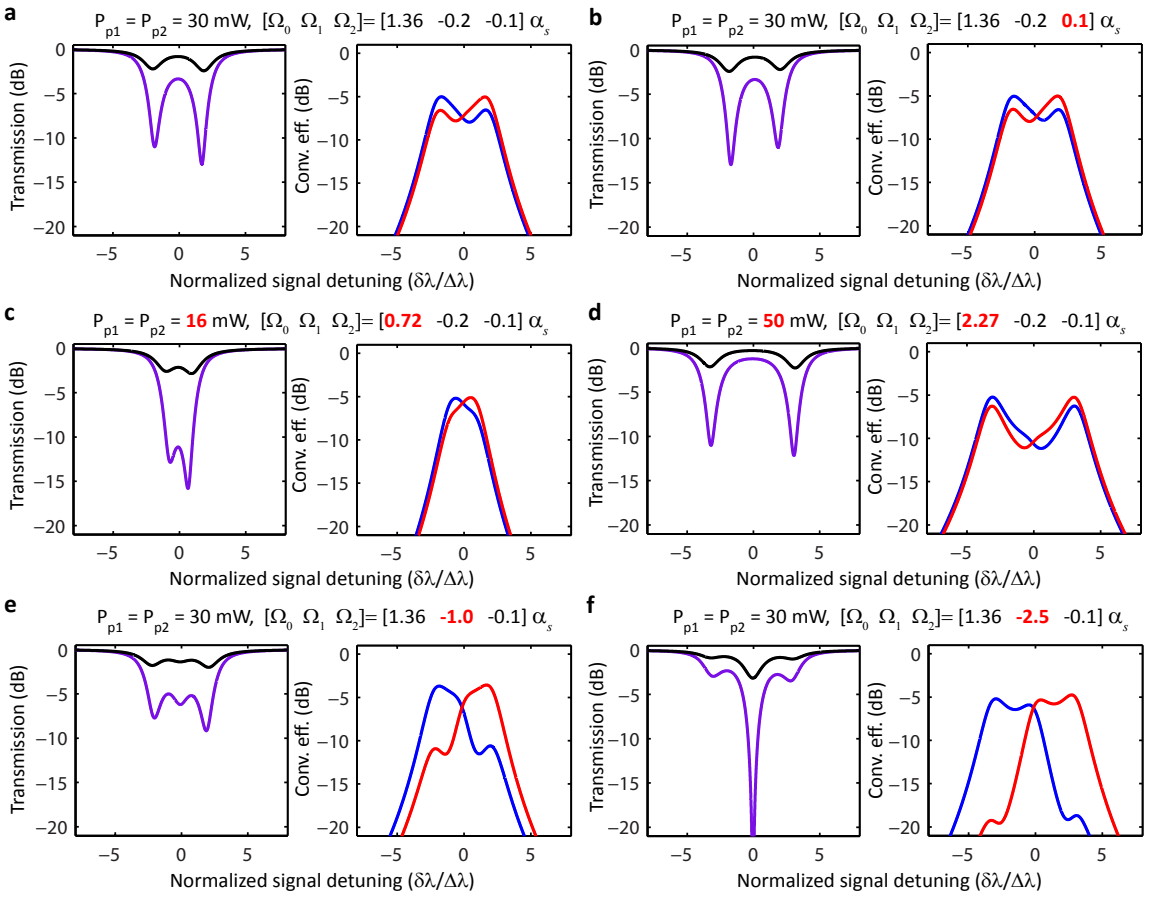

FIG. S3: **Coupled mode simulations for the 980 nm intraband conversion**. **a** Reference example of the parameter variations of $[\Omega_0\ \Omega_1\ \Omega_2]$ in units of α_s (cavity loss rate at the signal resonance). The varied parameter in other cases is highlighted. For each case, the left figure shows the transmission (purple: signal only; black: signal plus two idlers) and the right figure shows the on-chip conversion efficiency (blue for $i+$ and red for $i-$) as a function of normalized signal detunings ($-\Delta\phi_s/\alpha_s = \delta\lambda/\Delta\lambda$ where $2\Delta\lambda \approx 4$ pm is the linewidth of the signal resonance). **b**, Changing the sign of Ω_2 will reverse the symmetry between the two split modes in the transmission scan. **c-d**,Varying Ω_0 (i.e., the pump power): mode splitting increases with the pump power. **e-f**, Varying Ω_1: nonzero $|\Omega_1|$ removes the degeneracy in the conversion efficiency between $i+$ and $i-$; especially, a relatively large $|\Omega_1|$ can make one idler much stronger than the other at its optimum signal detuning.

conversion case since the two pumps are widely separated. Consequently, other than the two pumps, there are typically four modes: the signal (s), the auxiliary tone generated from the mixing of the signal and its nearby pump (s'), and two idlers ($i+$ and $i-$). The coupled mode equations developed here will only consider these four modes, which means we neglect higher order idlers generated from the mixing of $i\pm$ with its nearby pump.

To treat both the upconversion and downconversion, we label the two modes in the 980 nm band as a and b, and the two modes in the 1550 nm band as c and d (see Fig. S4). For the upconversion case, $[a\ b\ c\ d]$ correspond to $[i+\ i-\ s\ s']$, respectively. For the downconversion case, $[a\ b\ c\ d]$ correspond to $[s\ s'\ i+\ i-]$, respectively.

First, we consider the case without the signal input field driving its cavity resonance. The coupled mode equations for these four modes can be written as

$$t_R\frac{dE_a}{dt} = -(\alpha_{p1}+i\Delta\phi_a)E_a + i\gamma_{p1}LE_{p1}^2E_b^* + i2\gamma_{p1}LE_{p1}(E_{p2}E_d^* + E_{p2}^*E_c), \tag{28}$$

$$t_R\frac{dE_b}{dt} = -(\alpha_{p1}+i\Delta\phi_b)E_b + i\gamma_{p1}LE_{p1}^2E_a^* + i2\gamma_{p1}LE_{p1}(E_{p2}E_c^* + E_{p2}^*E_d), \tag{29}$$

$$t_R\frac{dE_c}{dt} = -(\alpha_{p2}+i\Delta\phi_c)E_c + i\gamma_{p2}LE_{p2}^2E_d^* + i2\gamma_{p2}LE_{p2}(E_{p1}E_b^* + E_{p1}^*E_a), \tag{30}$$

$$t_R\frac{dE_d}{dt} = -(\alpha_{p2}+i\Delta\phi_d)E_d + i\gamma_{p2}LE_{p2}^2E_c^* + i2\gamma_{p2}LE_{p2}(E_{p1}E_a^* + E_{p1}^*E_b), \tag{31}$$

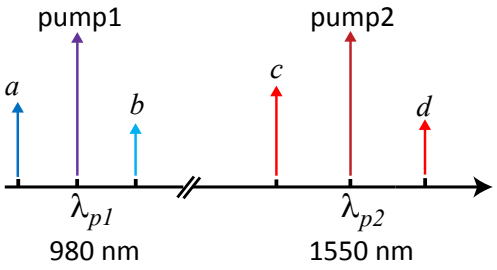

FIG. S4: **Schematic of the wideband conversion process.** This schematic shows the four modes under consideration in the coupled mode equations for the wideband frequency conversion. For the upconversion, c is the signal, d is the auxiliary tone resulting from the wave mixing between c and pump 2, and a and b are $i+$ and $i-$, respectively. For the downconversion, a is the signal, b is the auxiliary tone resulting from the wave mixing between a and pump 1, and c and d are $i+$ and $i-$, respectively.

where for simplicity we have approximated α and γ of each wave as the values of its nearby pump (e.g., $\gamma_{a,b}=\gamma_{p1}$ and $\gamma_{c,d}=\gamma_{p2}$). In addition, the effective detunings of these modes are obtained as

$$\Delta\phi_a = (\hat{\omega}_a-\omega_a)t_R - 2\gamma_{p1}L(|E_{p1}|^2+|E_{p2}|^2), \tag{32}$$
$$\Delta\phi_b = (\hat{\omega}_b-\omega_b)t_R - 2\gamma_{p1}L(|E_{p1}|^2+|E_{p2}|^2), \tag{33}$$
$$\Delta\phi_c = (\hat{\omega}_c-\omega_c)t_R - 2\gamma_{p2}L(|E_{p1}|^2+|E_{p2}|^2), \tag{34}$$
$$\Delta\phi_d = (\hat{\omega}_d-\omega_d)t_R - 2\gamma_{p2}L(|E_{p1}|^2+|E_{p2}|^2). \tag{35}$$

Similar to the 980 nm intraband conversion, the energy conservation condition (see Fig. 5 in the main paper) is used to express the detunings of the idlers as a function of the signal and pump detunings, which are free parameters to be varied in the experiment. For example, for the upconversion case, energy conservation requires $\omega_a=\omega_{p1}+|\omega_c-\omega_{p2}|$, $\omega_b=\omega_{p1}-|\omega_c-\omega_{p2}|$, and $\omega_d=2\omega_{p2}-\omega_c$. With some algebra, we arrive at

$$\Delta\phi_a = [(\hat{\omega}_a-\hat{\omega}_{p1})-(\hat{\omega}_c-\hat{\omega}_{p2})]t_R+\Delta\phi_c+(\Delta\phi_{p1}-\Delta\phi_{p2})-(\gamma_{p1}L|E_{p1}|^2-\gamma_{p2}L|E_{p2}|^2), \tag{36}$$
$$\Delta\phi_b = [(\hat{\omega}_b-\hat{\omega}_{p1})+(\hat{\omega}_c-\hat{\omega}_{p2})]t_R-\Delta\phi_c+(\Delta\phi_{p1}+\Delta\phi_{p2})-(\gamma_{p1}L|E_{p1}|^2+\gamma_{p2}L|E_{p2}|^2), \tag{37}$$
$$\Delta\phi_d = [\hat{\omega}_d+\hat{\omega}_c-2\hat{\omega}_{p2}]t_R-\Delta\phi_c+2\Delta\phi_{p2}-2\gamma_{p2}L|E_{p2}|^2. \tag{38}$$

In the same way, for the downconversion case (a is the signal), we have $\omega_c=\omega_{p2}+|\omega_a-\omega_{p1}|$, $\omega_d=\omega_{p2}-|\omega_a-\omega_{p1}|$, and $\omega_b=2\omega_{p1}-\omega_a$. The effective detunings of these modes can then be derived as

$$\Delta\phi_c = [(\hat{\omega}_c-\hat{\omega}_{p2})-(\hat{\omega}_a-\hat{\omega}_{p1})]t_R+\Delta\phi_a-(\Delta\phi_{p1}-\Delta\phi_{p2})+(\gamma_{p1}L|E_{p1}|^2-\gamma_{p2}L|E_{p2}|^2), \tag{39}$$
$$\Delta\phi_d = [(\hat{\omega}_d-\hat{\omega}_{p2})+(\hat{\omega}_a-\hat{\omega}_{p1})]t_R-\Delta\phi_a+(\Delta\phi_{p1}+\Delta\phi_{p2})-(\gamma_{p1}L|E_{p1}|^2+\gamma_{p2}L|E_{p2}|^2), \tag{40}$$
$$\Delta\phi_b = [\hat{\omega}_a+\hat{\omega}_b-2\hat{\omega}_{p1}]t_R-\Delta\phi_a+2\Delta\phi_{p1}-2\gamma_{p1}L|E_{p1}|^2. \tag{41}$$

Now we add back the driving field for the signal. By defining a vector $\tilde{E}_r=[E_a\ E_b^*\ E_c\ E_d^*]^T$ (the subscript r is to denote that they are fields inside resonator and the superscript T stands for transpose of a matrix), we can write Eqs. 28-31 into a more compact form as

$$t_R\frac{d\tilde{E}_r}{dt}=\tilde{M}\tilde{E}_r+i\sqrt{\tilde{\Theta}}\tilde{E}_{\text{in}}, \tag{42}$$

where the matrix $\tilde{M}$ is defined by

$$\tilde{M}\equiv\begin{bmatrix} -\alpha_{p1}-i\Delta\phi_a & i\gamma_{p1}LE_{p1}^2 & i2\gamma_{p1}LE_{p1}E_{p2}^* & i2\gamma_{p1}LE_{p1}E_{p2} \\ -i\gamma_{p1}LE_{p1}^{*2} & -\alpha_{p1}+i\Delta\phi_b & -i2\gamma_{p1}LE_{p1}^*E_{p2}^* & -i2\gamma_{p1}LE_{p1}^*E_{p2} \\ i2\gamma_{p2}LE_{p1}^*E_{p2} & i2\gamma_{p2}LE_{p1}E_{p2} & -\alpha_{p2}-i\Delta\phi_c & i\gamma_{p2}LE_{p2}^2 \\ -i2\gamma_{p2}LE_{p1}^*E_{p2}^* & -i2\gamma_{p2}LE_{p1}E_{p2}^* & -i\gamma_{p2}LE_{p2}^{*2} & -\alpha_{p2}+i\Delta\phi_d \end{bmatrix}, \tag{43}$$

$\tilde{\Theta}$ is a diagonal matrix defined as $\tilde{\Theta}\equiv\text{diag}(\theta_{p1}\ \theta_{p1}\ \theta_{p2}\ \theta_{p2})$, and $\tilde{E}_{\text{in}}$ is the driving field. For the upconversion case (mode c is the signal), $\tilde{E}_{\text{in}}=[0\ 0\ \sqrt{P_s}\ 0]^T$ and for the downconversion case (mode a is the signal), $\tilde{E}_{\text{in}}=[\sqrt{P_s}\ 0\ 0\ 0]^T$. The steady state

solution can be found from Eq. 42 as $\tilde{E}_r = -i\tilde{M}^{-1}\sqrt{\tilde{\Theta}}\tilde{E}_{\text{in}}$ for the fields inside cavity and $\tilde{E}_{\text{WG}} = \tilde{E}_{\text{in}} + i\sqrt{\tilde{\Theta}}\tilde{E}_r$ for the fields at the output of the waveguide. Note that each component of $|\tilde{E}_{\text{WG}}|^2$ represents the power of the corresponding mode, which has to be converted to photon flux for the calculation of the the on-chip conversion efficiency. Simulation examples are provided in Fig. S8c for the upconversion case and Fig. 6b in the main paper for the downconversion case, both showing a good agreement with the experimental results.

C. Modified LLE method for FWM-BS

In this subsection, we will discuss a way to adapt the conventional LLE method for the FWM-BS process. So far, the coupled mode equations presented only consider a few modes. For example, for the intraband conversion in the 980 nm band, we have neglected the pump mixing in the 1550 nm band as well as high-order idler generation in the 980 nm band. It is still possible to include these modes in the coupled mode equations, although the process is typically very manual. By contrast, the LLE formalism can automatically include all resonant modes for the entire wavelength band of interest, making it a convenient tool to study the interaction of multiple modes.

As pointed out at the beginning of this section, in the standard LLE formalism we only set the detuning of the pump (δ_0 in Eq. 7) which is the only driving field[17,18]. In addition, the resonance frequencies of all the modes are referenced to an equally spaced frequency grid $\{\omega_0 + D_1\mu\}$, with D_1 corresponding to the FSR of the pump resonance. In the FWM-BS process, since we have three driving fields (two pumps and one signal), it is not straightforward to allow these three waves have their own detunings independent from the others. In addition, it is also not trivial to choose D_1. For example, even if we decide D_1 should be the FSR of the resonator, we still face the choice of the FSR in the 1550 nm or the 980 nm band.

The solution we find is to implement the LLE formalism based on Eq. 8, whose detuning parameter ($\delta_m = \hat{\omega}_m - \omega_m$) is allowed to vary across different resonant modes. Thus, we can set δ_m corresponding to the two pumps and the signal. The detunings of the remaining modes are determined from the following procedure. First, we obtain resonance frequencies ($\{\hat{\omega}_m\}$) of all the modes from numerical simulations based on an eigenfrequency mode solver for the microresonator under study; second, the equally spaced frequency grid ($\{\omega_m\}$) is set up in the 1550 nm and 980 nm bands separately before joining together. To make it clear, we use the 980 nm intraband conversion as an example (Fig. S4). Assuming the 1550 nm pumps are accommodated by two resonances adjacent to each other (i.e., $m_{p1} - m_{p2} = 1$), the frequency grid in the 980 nm band is chosen as $\omega_m = \omega_s + (m - m_s)|\omega_{p1} - \omega_{p2}|$, where m_s is the azimuthal order of the signal resonance. By doing so, the signal and all the generated idlers automatically fall on the frequency grid (energy conservation satisfied). Similar to the situation in the coupled mode equations, here ω_s, ω_{p1} and ω_{p2} can be replaced by their respective detunings ($\omega_m = \hat{\omega}_m - \delta_m$). Likewise, in the 1550 nm band, we can start with either pump and expand the grid with the same spacing (i.e., $|\omega_{p1} - \omega_{p2}|$). This allows the two 1550 nm pumps and secondary pumps generated from pump mixing to be on the grid, since the energy conservation is automatically satisfied. Finally, we expand the frequency grid in the 980 nm band and the one in the 1550 nm band until they start to overlap the middle of the total frequency span (typically we consider a wavelength range from 900 nm to 1700 nm, so the midpoint is around 1200 nm). Admittedly, there could be some error for the detuning of the joint point (basically ω_m extended from the 980 nm grid is not necessarily equal to that from the 1550 nm grid), but generally this mode is frequency mismatched and far away from the wavelength bands that interest us. As a result, we end up with a frequency grid that spans the whole spectral range, and all the modes of interest are on the grid. Following the same reasoning, if the two 1550 nm pumps are accommodated by resonances with their azimuthal order difference $N = |m_{p1} - m_{p2}| > 1$, we should take the grid spacing as $|\omega_{p1} - \omega_{p2}|/N$. Similarly, for the wideband conversion case, the grid spacing is taken as the frequency difference between the signal and its nearby pump, divided by the difference of their azimuthal orders. Therefore, we can clearly see from this process that the frequency grid spacing is not exactly the FSR of the resonator, with the deviation contributed by nonzero detuning and high-order dispersions.

From the discussion, it should be clear by now that the modified LLE method described above is essentially a systematic way to implement the coupled mode equations discussed in previous subsections (A and B), so that all the resonant modes can be included easily. Other than the detuning, parameters such as α, γ, and θ in Eq. 8 can (and should) be frequency dependent. To solve Eq. 8 numerically, we use the well-known split-step Fourier method, i.e., we calculate the frequency-dependent terms (Eq. 8 without the nonlinear Fourier transformed term) in the frequency domain and then compute the nonlinear term in the time domain. The implementation is similar to that described in Ref. 2.

D. Calculation of Kerr nonlinear coefficient

The purpose of this subsection is to provide a brief discussion on the calculation of the Kerr nonlinear coefficient γ in a nanophotonic structure, as we have noticed there are several different versions existing in the literature [2,22]. We will consider only one wave (the pump) here, as it is fairly straightforward to generalize the result to multiple waves [23,24]. The most common version for γ is probably $\gamma = \frac{n_2\omega}{cA_{\text{eff}}}$ (Ref. 2), where n_2 is the Kerr nonlinear refractive index ($n_2 \approx 2.5 \times 10^{-19}$ m^{2}W^{-1} for Si_3N_4),

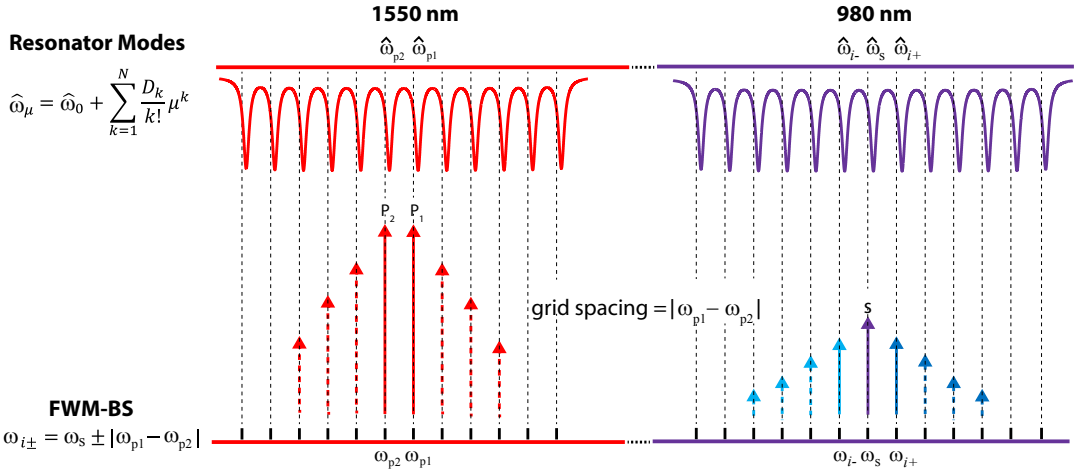

FIG. S5: **Schematic of the frequency grid used in the LLE simulation.** The frequency grid shown here corresponds to the 980 nm intraband conversion with two 1550 nm band pumps accommodated by two adjacent resonances. The vertical dashed arrows in the 1550 nm and 980 nm band represent the secondary pumps generated from the pump mixing and high-order idlers, respectively. The resonator modes are illustrated above, indicating the resonance frequencies are not exactly on the grid due to non-zero detuning and high-order dispersions.

and A_{eff} is the effective mode area given by

$$A_{\text{eff}} = \frac{\left(\int\int |\mathbf{E}(x,y)|^2\, dxdy\right)^2}{\int\int_{\text{core}} |\mathbf{E}(x,y)|^4\, dxdy}, \tag{44}$$

where $\mathbf{E}(x,y)$ is the electric field of the mode under consideration, and the subscript in the integral denotes the integral over the nonlinear (core) material. This result is typically applied to fibers or waveguides with low index contrast materials.

It is expected that Eq. 44 requires some modification when applied to nanophotonic structures with high index contrast material systems (such as Si_3N_4/SiO_2, Si/SiO_2 or $AlGaAs/SiO_2$). For the $\chi^{(3)}$ process in a microresonator, it has been shown that the effective mode volume is given by [22]

$$V_{\text{eff}} = \frac{\left(\int\int\int \varepsilon_r(\mathbf{r})|\mathbf{E}(\mathbf{r})|^2\, d^3\mathbf{r}\right)^2}{\int\int\int_{\text{core}} \varepsilon_r^2(\mathbf{r})|\mathbf{E}(\mathbf{r})|^4\, d^3\mathbf{r}}, \tag{45}$$

where ε_r is the relative permittivity. Following this, one may naturally expect that for a waveguide,

$$\bar{A}_{\text{eff}} = \frac{\left(\int\int \varepsilon_r(x,y)|\mathbf{E}(x,y)|^2\, dxdy\right)^2}{\int\int_{\text{core}} \varepsilon_r^2(x,y)|\mathbf{E}(x,y)|^4\, dxdy}. \tag{46}$$

On the other hand, we can start with the variational principle[25], that is,

$$\delta\beta = \frac{\omega \int\int_{\text{core}} \mathbf{E}^*(x,y)\cdot\mathbf{P}(x,y)\, dxdy}{4P_o}, \tag{47}$$

where $\mathbf{P}(x,y)$ is the dielectric perturbation and P_o is the power of the waveguide. For the $\chi^{(3)}$ process involving only one wave, we have $\mathbf{P}(x,y) = 3\varepsilon_0\chi^{(3)}_{1111}|\mathbf{E}(x,y)|^2\mathbf{E}(x,y)/4$, where ε_0 is the vacuum permittivity and $\chi^{(3)}_{1111}$ is related to n_2 as $n_2 = 3\chi^{(3)}_{1111}/(4n_0^2\varepsilon_0 c)$ (Ref. 26), with n_0 being the refractive index of the material. One can easily observe that the nonlinear perturbation results in a power-dependent $\delta\beta$, which is recognized as the self phase modulation. Hence, $\delta\beta = \gamma P_o$. As a result, we end up with $\gamma = \frac{n_2\omega}{c\tilde{A}_{\text{eff}}}$, with a new mode area $\tilde{A}_{\text{eff}}$ defined as

$$\tilde{A}_{\text{eff}} = \frac{4P_o^2}{n_0^2\varepsilon_0^2 c^2 \int\int_{\text{core}} |\mathbf{E}(x,y)|^4\, dxdy}. \tag{48}$$

Since the power of the waveguide mode is given by an integral of mode energy density over the waveguide cross section multiplied by the group velocity, we can simplify $\tilde{A}_{\text{eff}}$ as

$$\tilde{A}_{\text{eff}} = \left(\frac{n_0}{n_g}\right)^2 \frac{\left(\int\int \varepsilon_r(x,y)|\mathbf{E}(x,y)|^2\, dxdy\right)^2}{\int\int_{\text{core}} \varepsilon_r^2(x,y)|\mathbf{E}(x,y)|^4\, dxdy}, \tag{49}$$

which shows there is an additional factor $(n_0/n_g)^2$ compared to $\bar{A}_{\text{eff}}$ in Eq. 46.

We want to point out Eq. 45 is derived based on the same variational principle as Eq. 49. On the other hand, we believe it is not strictly valid to go from Eq. 45 to Eq. 46 for two reasons. First, Eq. 45 is derived for modes with normalized energy, while for waveguides we are dealing with modes normalized by power. The conversion from energy to power introduces a factor proportional to the round-trip time ($t_R = Ln_g/c$) for the $\chi^{(3)}$ nonlinear term. Second, what has been calculated for the waveguide case is $\delta\beta$ caused by the nonlinear perturbation, while the counterpart for the cavity case is the frequency shift $\delta\omega$. They are related by $\delta\beta \approx n_g\delta\omega/c$. Thus, it seems the $(n_0/n_g)^2$ factor can be explained. Nevertheless, for the Si_3N_4 waveguides (that form the ring resonator) studied in this work, the numerical value of $\bar{A}_{\text{eff}}$ is almost the same as $\tilde{A}_{\text{eff}}$, since $n_g \approx n_0 \approx 2$. In comparison, the calculated γ is about 35 % higher than the result based on Eq. 44, suggesting it is important to choose the right mode area for the numerical simulation.

IV. SUMMARY OF PARAMETERS AND NUMERICAL RESULTS FOR FWM-BS SIMULATION

TABLE S4: Parameters used in the simulations

Parameter	1550 nm band	980 nm band	Unit	Source
Q_i	4.5×10^5	9.0×10^5	-	Low-power transmission measurement
Q_c	2.3×10^5	3.3×10^5	-	Low-power transmission measurement
Q_L	1.5×10^5	2.4×10^5	-	Low-power transmission measurement
$D_1/2\pi$	572.39	572.25	GHz	Low-power transmission measurements across multiple resonances
$D_2/2\pi$	-31.04	-3.43	MHz	Low-power transmission measurements across multiple resonances
$D_3/2\pi$	0.71	-0.30	MHz	Low-power transmission measurements across multiple resonances
γ	2.07	3.32	$W^{-1}m^{-1}$	FEM simulations

We list the parameters used in the FWM-BS simulations in table S4. In addition, in Fig. S6 we provide the mode profiles of the fundamental TE mode of the access waveguide and ring waveguide in both the 1550 nm and 980 nm bands. Note that the access waveguide supports 1 TE mode and 1 TM mode in the 1550 nm band, and 2 TE modes and 2 TM modes in the 980 nm band. On the other hand, the ring waveguide supports 2 TE modes (though the second-order TE mode is close to cut off) and 1 TM mode in the 1550 nm band, and at least 3 TE modes and 3 TM modes in the 980 nm band. Our work involves the fundamental TE modes, and due to a general lack of spectral and spatial overlap with the other modes, as well as selective excitation of the desired TE modes by the pulley coupler (see Section V), the existence of other modes does not play a significant role in our measurements (except at some particular wavelengths). The propagation loss of the fundamental TE mode in the waveguide is estimated to be less than 1 dB/cm in both the 1550 nm and 980 nm bands.

V. TRANSMISSION MEASUREMENTS

To characterize the resonances of the microring device in the 1550 nm band, two tunable lasers covering wavelength ranges from 1415 nm to 1480 nm and 1520 nm to 1570 nm are employed. Figure S7a shows the measured transmission (defined as the power collected by the lens fiber from the waveguide output normalized by the power sent to the lens fiber that couples to the waveguide input). As can be seen, even though the microring is multimode, only the fundamental TE mode is observed in the transmission spectrum, thanks to the pulley coupling design[27]. Figure S7b shows the transmission scan of the resonance around 1550 nm. At low powers, the resonance shape is close to Lorentzian; as the power increases, thermo-optic dispersion quickly results in the swept-wavelength lineshape following the commonly observed thermal triangle.

Figure S7c shows the transmission of the 980 nm band, whose characterization involves three tunable lasers. The first two lasers, which have been used as the signal in the downconversion experiment (Fig. 6a in the main paper), cover wavelength ranges from 930 nm to 955 nm and 960 nm to 990 nm. The third laser, which has been used as the 980 nm pump for the wideband conversion experiment, has a tunable wavelength range from 915 nm to 985 nm and a relatively large output power ($\approx$ 45 mW). Considering $\approx$ 6.5 dB coupling loss at the input facet, the maximum on-chip pump power is limited to $<$ 10 mW. Similar to the 1550 nm spectrum, the transmission of the 980 nm band shows that only the fundamental TE mode is well-coupled while other modes are suppressed. However, as illustrated by Fig. S7d, the fundamental TE mode can interact with some other mode at certain wavelengths, which shifts its resonance frequency as shown in Fig. 2f in the main paper. By changing the polarization

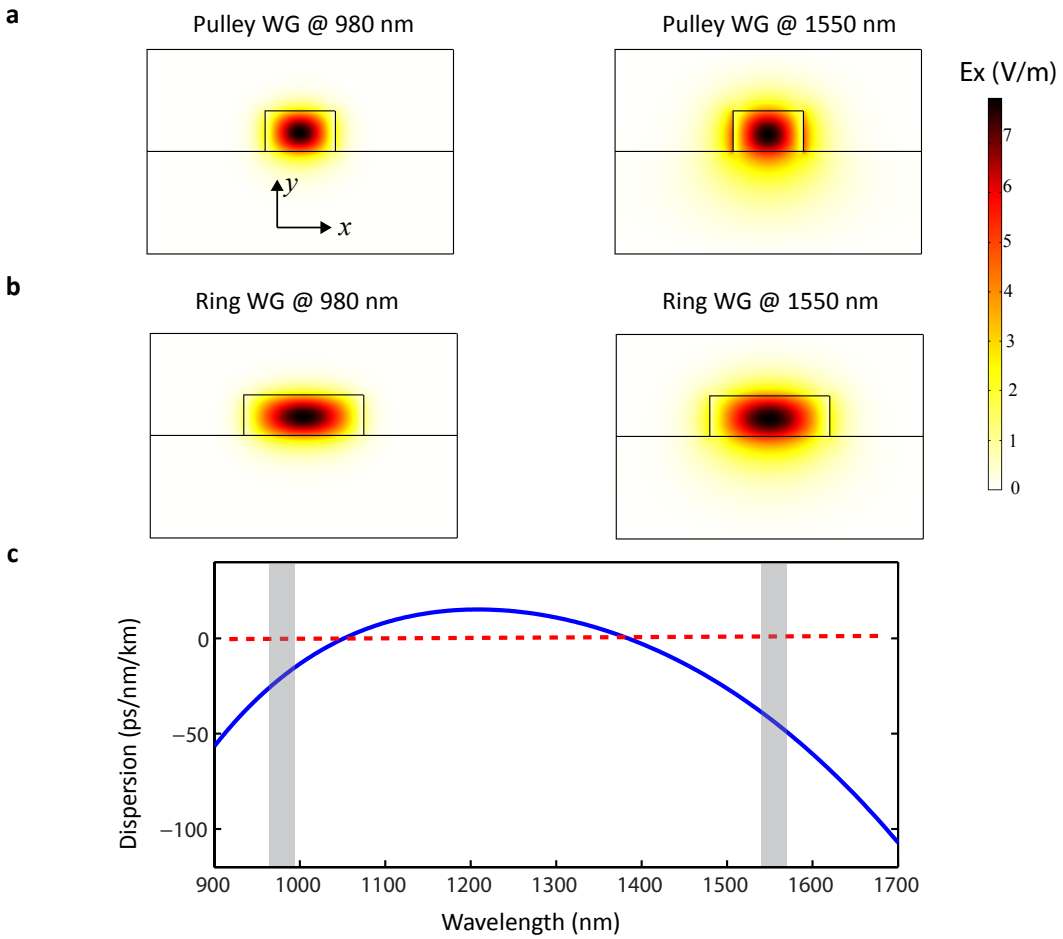

FIG. S6: **Mode profiles and resonator dispersion.** Electric field (x component) of the fundamental TE mode in the 980 nm band (left) and 1550 nm band (right) for **a**: access waveguide with width of 820 nm and height of 480 nm, and for **b**: ring waveguide with width of 1400 nm and height of 480 nm. **c** An enlarged version of the microring's dispersion shown in Fig. 4a in the main paper: the 980 nm and 1550 nm bands are highlighted and shown to be in the normal dispersion regime.

state of the input light, we find we can increase the extinction ratio of the mode that couples to the TE resonance, suggesting this mode has a different polarization. Through a careful phase-matching analysis, we believe the mode is most likely to be the fundamental TM mode. Such excitation is possible because the TE waveguide mode has a nonzero field overlap with the TM mode of the resonator, though generally the coupling is weak and only strong at certain wavelengths due to an accidental phase matching.

VI. 1550 NM TO 980 NM UPCONVERSION: ADDITIONAL DISCUSSIONS

The experimental setup for the 1550 nm to 980 nm upconversion is shown in Fig. S8a, where a 1550 nm laser is amplified by the EDFA (pump), combined with another 1550 nm laser (signal), and then combined with the 980 nm pump before being coupled to the frequency conversion chip. Figure S8b shows some representative OSA spectra in the 980 nm band as we vary the spectral separation between the signal and the 1550 nm pump, while keeping the pump configuration the same as the example shown in Fig. 5b in the main paper (which corresponds to 8 FSR separation). By examining Eq. 36 (effective detuning of $i+$ in upconversion) and Eq. 39 (effective detuning of $i+$ in downconversion), we find the frequency detuning of $i+$ is essentially the same for the upconversion and downconversion schemes (except that the sign is opposite), suggesting similar performance for $i+$ between the two cases in terms of conversion efficiency and bandwidth. This is confirmed by comparing the experimental data to the simulation results based on the coupled mode equations as discussed in Section III.B (Fig. S8c). On the other hand, the frequency detuning for $i-$ (Eq. 37) is significantly different from the downconversion case (Eq. 40), which seems to indicate that $i-$ should have similar conversion efficiencies as $i+$ even for reasonably large $|\mu|$ values. However, the measured conversion efficiencies are much worse than the simulation results (Fig. S8c). The discrepancy can be attributed to several factors. First, some resonances accommodating $i-$ have been shifted in the spectrum by mode interactions (such as $\mu = -2, -3$, see Fig. 2f in

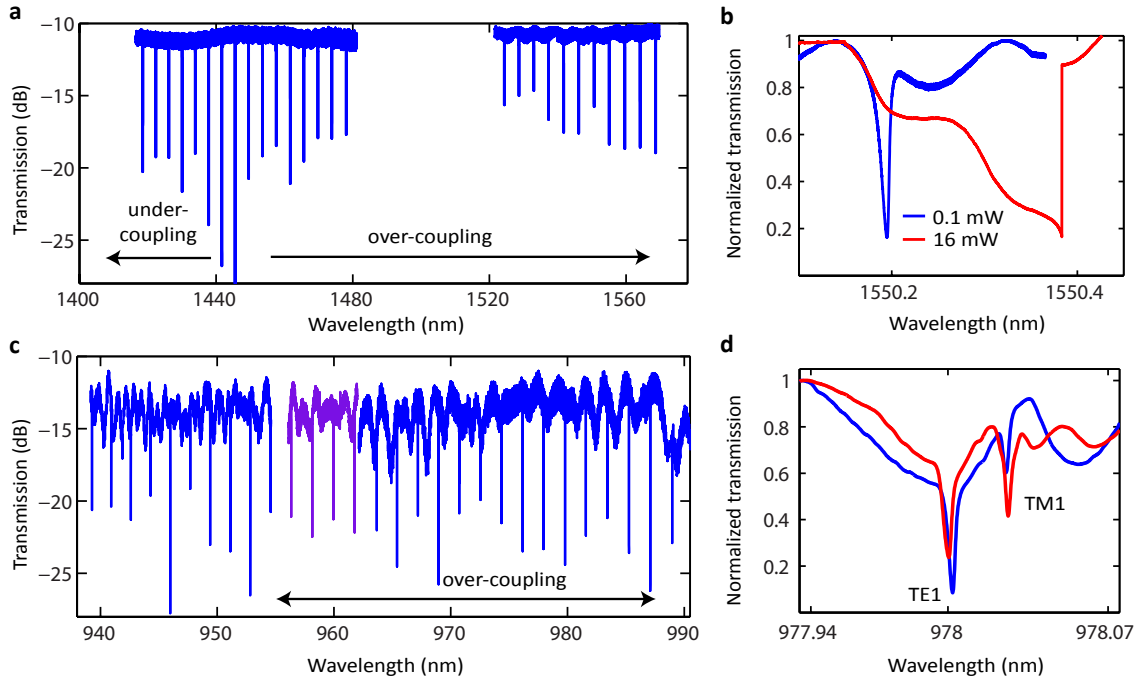

FIG. S7: **Transmission measurement of the microring device**. **a**, Transmission of the microring measured with tunable lasers covering wavelength ranges from 1415 nm to 1480 nm and 1520 nm to 1570 nm. **b**, Normalized transmission scan of the resonance around 1550 nm at a low power (0.1 mW, showing a very slight thermal triangle) and high power (16 mW, showing a very strong thermal triangle). **c**, Transmission of the microring measured with tunable lasers (blue lines) from 939 nm to 955 nm and 962 nm to 990 nm. The resonances in the wavelength gap (purple line) are measured by a third tunable laser covering wavelength range from 915 nm to 985 nm. **d**, Normalized transmission scan of the 978 nm resonance (power = 0.1 mW) when the polarization is TE (blue) and slightly away from TE (red).

the main paper), which cause large frequency detunings that are not accounted for in the simulation. Second, the transmission at certain resonances (such as $\mu = -8$, see Fig. S7c) is much worse than other resonances, possibly due to some resonant scattering from defects along the waveguide or on the cleaved facets, leading to less power in the transmitted idlers. Finally, the frequency detuning of the two pumps can drift during the experiment, which impacts the two idlers in a different way. The 1550 nm pump is always blue detuned (i.e., $\Delta\phi_{p2} < 0$), since otherwise the thermal lock will be lost and no conversion efficiency will be observed. On the other hand, the 980 nm pump exhibits a Lorentzian transmission scan due to the fact that its power is much smaller compared to the 1550 nm pump. Though in the experiment we try to set $\Delta\phi_{p1} \approx 0$ by parking the laser to its minimum of transmission, it has been observed that the 980 nm pump can often drift away from the initial position within a relatively short time. As can be seen from the simulation shown in Fig. S8d, $i-$ is much more sensitive to the pump detunings than $i+$ for the device under study, especially to the detuning of the 980 nm pump.

VII. 980 NM TO 1550 NM DOWNCONVERSION: ADDITIONAL DISCUSSIONS

The experimental setup for the 980 nm to 1550 nm downconversion is shown in Fig. S9a, where we have added a narrowband filter (bandwidth $\approx$ 100 GHz) after the EDFA to remove the ASE noise. In addition, cascaded WDM filters have been used at the detection side to reject the 1550 nm pump ($>$ 120 dB suppression) while allowing idlers to pass with a small insertion loss ($\approx$ 3 dB). The transmitted idlers are bandpassed by a narrowband filter with a tunable bandwidth (32 pm to 600 pm, , see Fig. S11a for its transmission response) and center wavelength (1460 nm to 1560 nm) before detection by a SPAD. Figure S9 shows the OSA spectra by varying the 1550 nm pump power while keeping the 980 pump power fixed. (The pump and signal configuration is the same as the example shown in Fig. 5d in the main paper.) As can be seen, the extinction ratio of the signal resonance increases with the 1550 nm pump power (left figure), while the generated idler $i+$ increases initially and then saturates (right figure). The summarized conversion efficiency of $i+$ versus the 1550 nm pump power shown in Fig. S9c indicates the conversion efficiency scales linearly with the 1550 nm pump power, which is expected as the the conversion efficiency is determined by the product of two pump powers[12] (see Eq. 43).

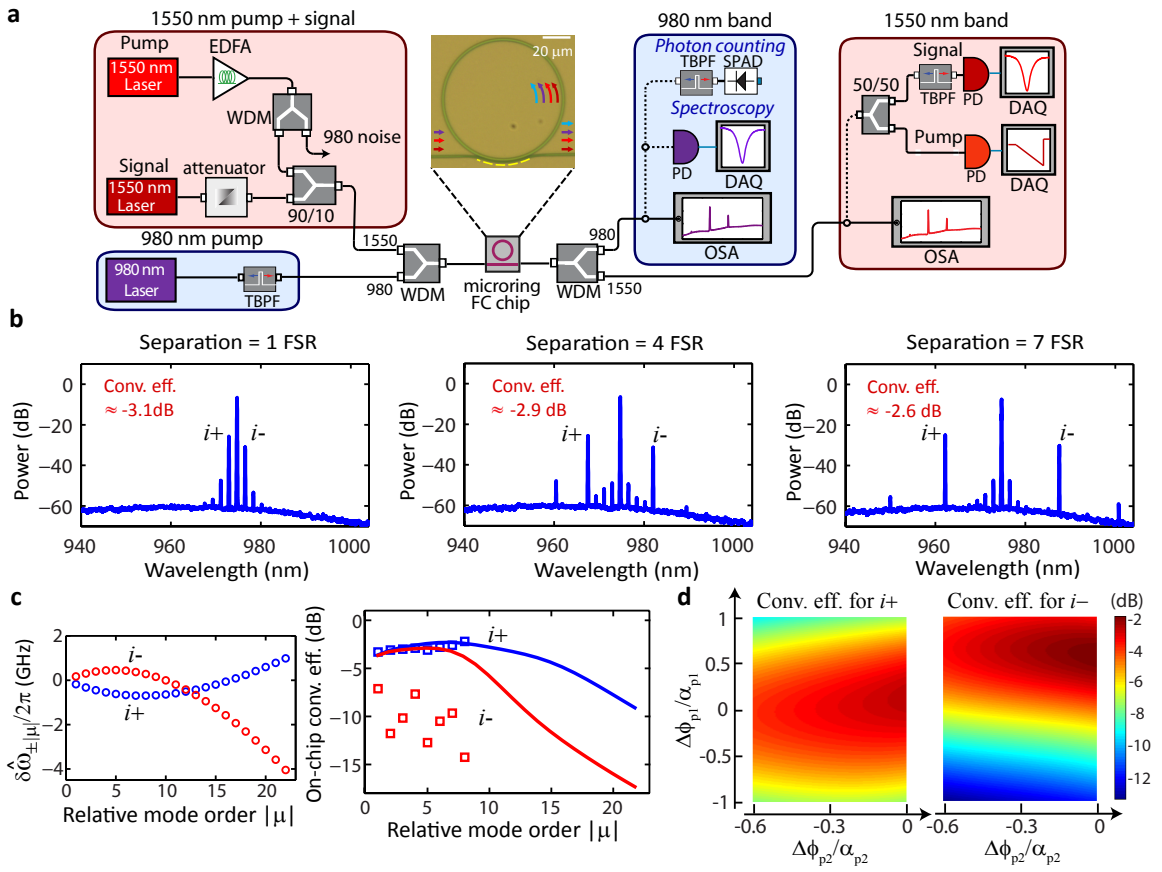

FIG. S8: **Experimental setup and additional data for upconversion**. **a**, Experimental setup for the frequency upconversion from the 1550 nm band to the 980 nm band. **b**, Representative 980 nm OSA spectra of upconversion for different frequency separations between the signal and the 1550 nm pump while keeping the pump configuration fixed: the two pumps in the 980 nm and 1550 nm bands are located at 974.4 nm (power ≈ 8 mW) and 1564.5 nm (power ≈ 50 mW), respectively. A power of 0 dB is referenced to 1 mW. **c**, The left figure shows the calculated frequency detunings for $i+$ and $i-$ at different idler positions, and the right figure compares the measured (markers) and simulated (solid lines) on-chip conversion efficiencies for $i+$ and $i-$ as we vary the separation between the signal and the 1550 nm pump. The error bars for the measured conversion efficiencies due to estimation uncertainties are less than the marker size. In the simulation, $\Delta\phi_{p1}/\alpha_{p1} = 0$ and $\Delta\phi_{p2}/\alpha_{p2} = -0.1$, where α_{p1} and α_{p2} are the cavity loss parameters for the 980 nm and 1550 nm pump, respectively. **d**, Simulated conversion efficiency for $i+$ (left) and $i-$ (right) as a function of the two pump detunings, $\Delta\phi_{p1}$ (980 nm pump) and $\Delta\phi_{p2}$ (1550 nm pump).

VIII. BACKGROUND NOISE MEASUREMENTS

In this section, we provide additional data on the background noise measurements performed in this work. Figure S10a shows the measured transmission response (blue curve) of the tunable bandpass filter used in the noise measurement for the 980 nm intraband conversion (Fig. 4e in the main paper), which consists of a 980 nm bandpass filter with a tunable center wavelength from 970 nm to 990 nm and a fixed bandwidth of 0.4 nm, and a longpass filter which suppresses light below 930 nm (≈ 1 dB insertion loss to light with wavelengths > 930 nm). It is found that when the 1550 nm pumps are on resonance, the noise measured by the SPAD can increase significantly (more than tenfold increase) if we remove the 930 nm longpass filter, indicating the majority of the noise is below the wavelength of 930 nm. Inspecting the 980 nm bandpass filter with a supercontinuum white light source and an OSA reveals that the bandpass filter has a wide passband below 820 nm (red curve in Fig. S10a), suggesting the excessive noise (without the 930 nm longpass) is likely to have wavelengths below 820 nm. Figure S10b shows the noise spectrum measured by a grating spectrometer with a sensitive (3 photoelectrons/count) CCD camera, revealing that there is a second harmonic signal generated by the 1560 nm pump around 780 nm. Note that such second harmonic generation from Si_3N_4 microrings has been observed in other experiments[28], and the $\chi^{(2)}$ effect is induced by the nanoscale structure of the waveguide which breaks the bulk symmetry of Si_3N_4. In our device, since the frequency mismatch for the the second harmonic generation is likely to be very large, the generated signal is very small (≈ 0.1 pW on chip). In addition, this signal can be easily filtered out (as we have done with the 930 nm longpass filter), since it is spectrally isolated from the wavelength band of interest (i.e., 980 nm band). The origin of the residual noise in the 980 nm band is still under investigation, though its magnitude (few fW

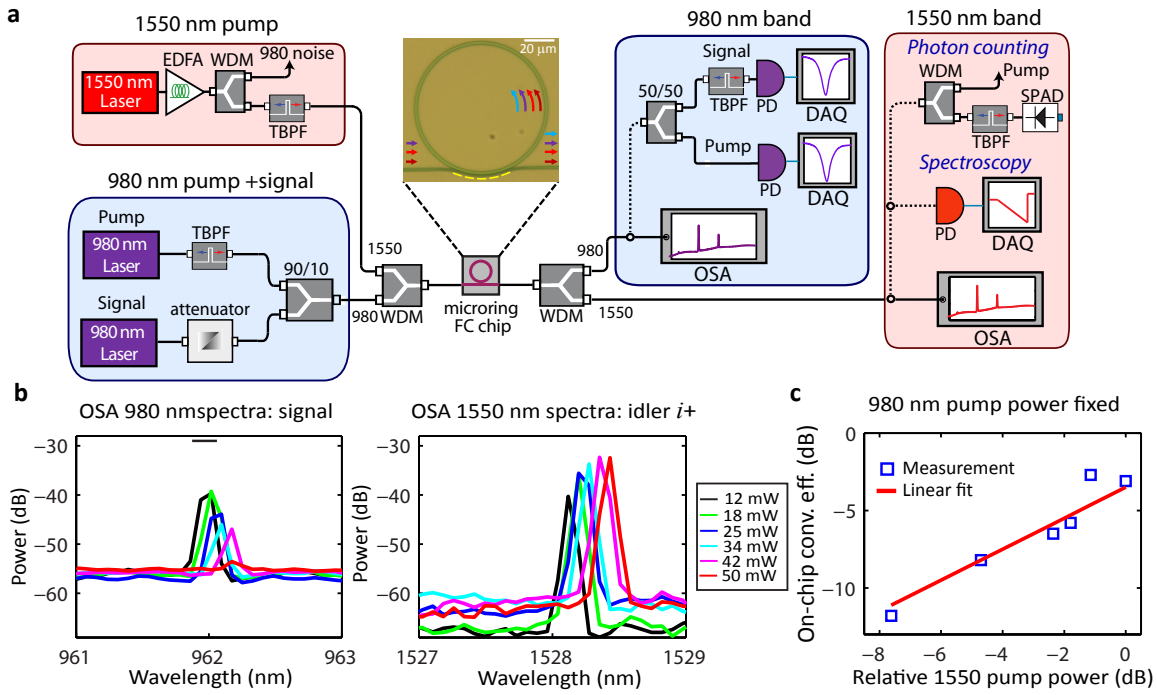

FIG. S9: **Experimental setup and additional data for downconversion**. **a**, Experimental setup for the frequency downconversion from the 980 nm band to the 1550 nm band. **b**, Superimposed OSA spectra for the 980 nm signal (left) and the 1550 nm idler $i+$ (right) corresponding to various 1550 nm pump powers (located at 1559.8 nm) and a fixed 980 nm pump power around 8 mW (located at 974.4 nm). The small horizontal bar in the left figure marks the signal off-resonance power (≈ -29 dB), where a power of 0 dB is referenced to 1 mW. **c**, Extracted conversion efficiencies for $i+$ from **b** (markers) plotted against a linear fit (solid line), showing that the conversion efficiency is proportional to the 1550 nm pump power. The error bars for the measured conversion efficiencies due to estimation uncertainties are less than the marker size. A power of 0 dB in the x axis is referenced to the maximum power used in the experiment (50 mW).

as measured in Fig. 4e in the main paper using a SPAD) is too small to be spectrally resolved using our grating spectrometer system.

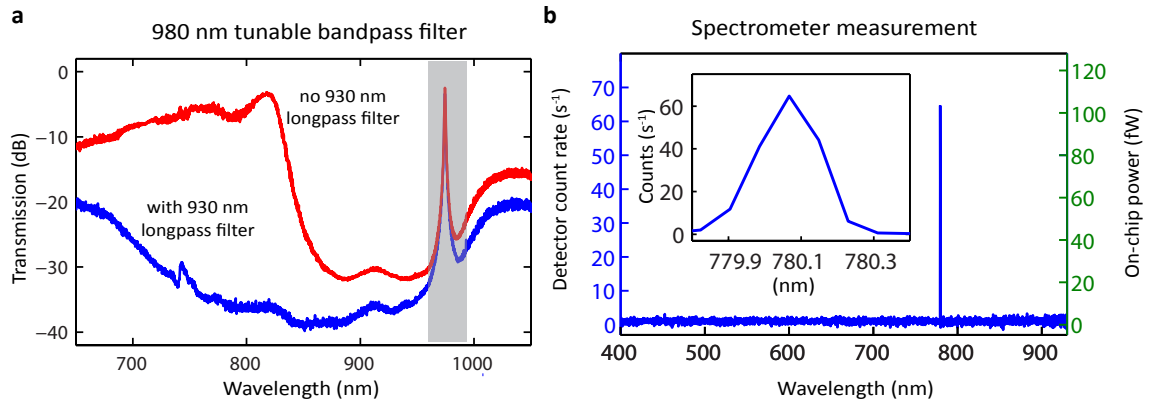

FIG. S10: **a**, Filter response of the tunable bandpass filter used for the background noise measurement in the 980 nm intraband conversion experiment (Fig. 4e in the main paper). The passband that is used for the selection of the idler is highlighted. The blue and red curve corresponds to the response of the filter with and without a 930 nm longpass filter, respectively. **b**, Spectrum of the noise generated by a strong 1550 nm pump with approximately 50 mW power on chip. The pump wavelength is around 1560.2 nm when it is thermally locked to the cavity resonance.

Next, we move on to discuss the noise in the 1550 nm band, in the context of the wideband downconversion measurements. Figure S11a shows the transmission responses of the narrowband filter used for the noise measurement in the frequency down-

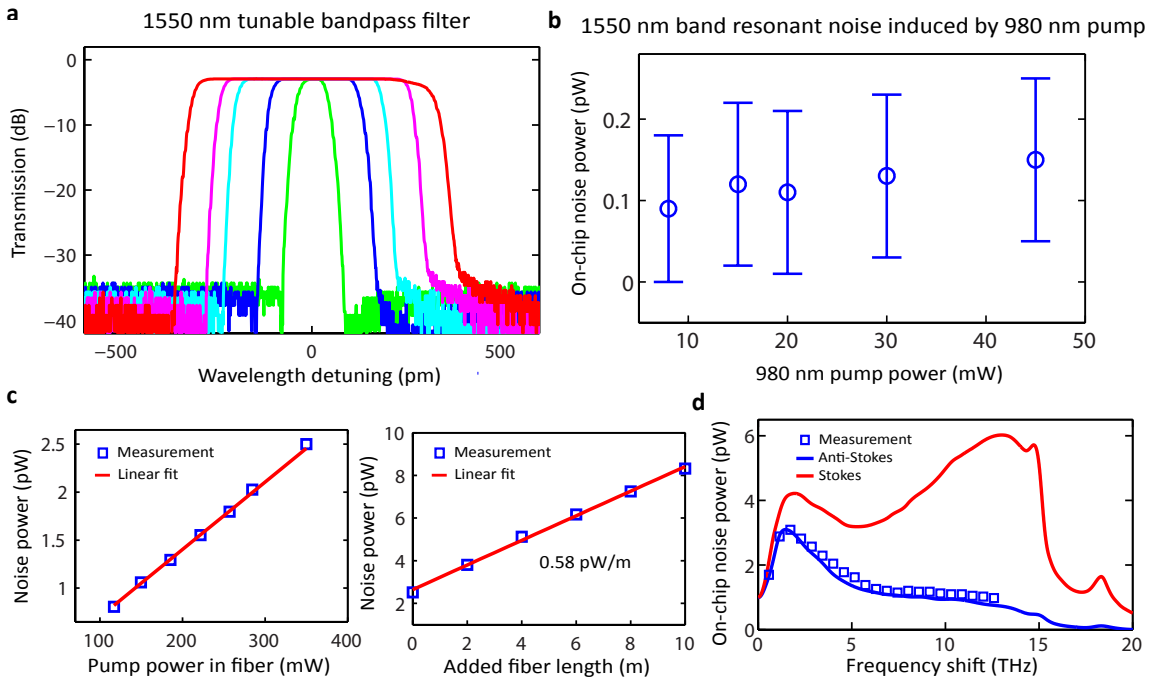

FIG. S11: **a**, Representative filter responses of the bandpass filter used for the background noise measurement in the downconversion experiment (Figs. 6c and 6d in the main paper), showing that its bandwidth can be tuned from 80 pm to 600 pm with almost the same insertion loss. **b**, Resonant noise measured at the 1528 nm resonance when the 980 nm pump is tuned into resonance (located at 974.4 nm). **c**, Background noise measured at the output of the narrowband filter after the EDFA at the input side (see Fig. S9a) as a function of the pump power in the fiber (left) and added fiber length for a fixed pump power around 350 mW in the fiber (right). On the detection side, the bandpass filter is set at 1528 nm (pump located at 1559.8 nm) with a filtering bandwidth of 80 GHz for both cases. **d**, The markers are the measured on-chip noise when the 1550 nm pump is off resonance for a detection bandwidth of 80 GHz (data re-plotted from Fig. 6c in the main paper as a function of the frequency shift from the pump), while the solid lines are the spontaneous Raman noise spectra from fibers for Stokes (red) and anti-Stokes (blue) sidebands [2,23,29,30]. The error bars in **b** are due to the fluctuation of the detected count rate by the InGaAs SPAD, and represent a one standard deviation value. The error bars in **c**-**d** are smaller than the marker size.

conversion experiment (Figs. 6c and 6d in the main paper), which is used to bandpass filter the downconverted idler in the 1550 nm band before the detection by a SPAD. The filter has a tunable bandwidth of 32 pm to 600 pm (although below 80 pm the insertion loss starts to increase), and a tunable center wavelength from 1460 nm to 1560 nm. Figure S11b plots the measured noise in the 1550 nm band induced by the 980 nm pump (in these measurements, the available 980 nm pump power is increased using a tunable Ti:sapphire laser). As can be seen, indeed the 980 nm pump generates little noise (< 0.2 pW on chip) in the 1550 nm band, thanks to the large spectral separation between these two bands. Since this is more than one order of magnitude smaller than the noise generated by the 1550 nm pump (Fig. 6d in the main paper), we focus on the latter as the dominant noise source to consider.

As mentioned in the main paper, when the 1550 nm pump is off resonance, we find a broadband noise that scales with the detection bandwidth and is linearly dependent on the pump power. Moreover, the measured noise is almost the same if we remove the chip and introduce a similar insertion loss between the two lensed fibers, strongly suggesting the noise is from the fiber itself. Figure S11c measures the noise at a fixed frequency shift (≈ 4 THz) from the pump at the input side (no chip), showing that the measured noise is linearly proportional to the pump power in the fiber (left figure) and increased fiber length for a fixed pump power (right figure). The extracted ratio of the increased noise power with the fiber length (≈ 0.58 pW/m) is consistent with the anti-Stokes Raman signal for a pump power of 350 mW with a detection bandwidth of 80 GHz [2]. To further support this argument, we re-plot the pump-off-resonance noise shown in Fig. 6c in the main paper in Fig. S11d (markers) as a function of the frequency shift, and compare it to the spontaneous anti-Stokes Raman spectrum (blue line, multiplied by a factor to match its peak power to that of the pump-off-resonance noise). The excellent agreement of the spectral shape confirms that the pump-off-resonance noise is mostly likely the anti-Stokes Raman signal generated inside the fiber.

In addition to the data shown in the main paper (Figs. 6c and 6d) for the resonant noise generated by the 1550 nm pump, we also study it using a grating spectrometer equipped with a liquid-nitrogen-cooled InGaAs photodiode array (sensitivity of 65 photoelectrons/count). Figure S12 has examples for two different pump powers, which show qualitative agreement with the method used in the main paper (i.e., spectral filtering + InGaAs SPAD). In principle, it is possible to extract the on-chip

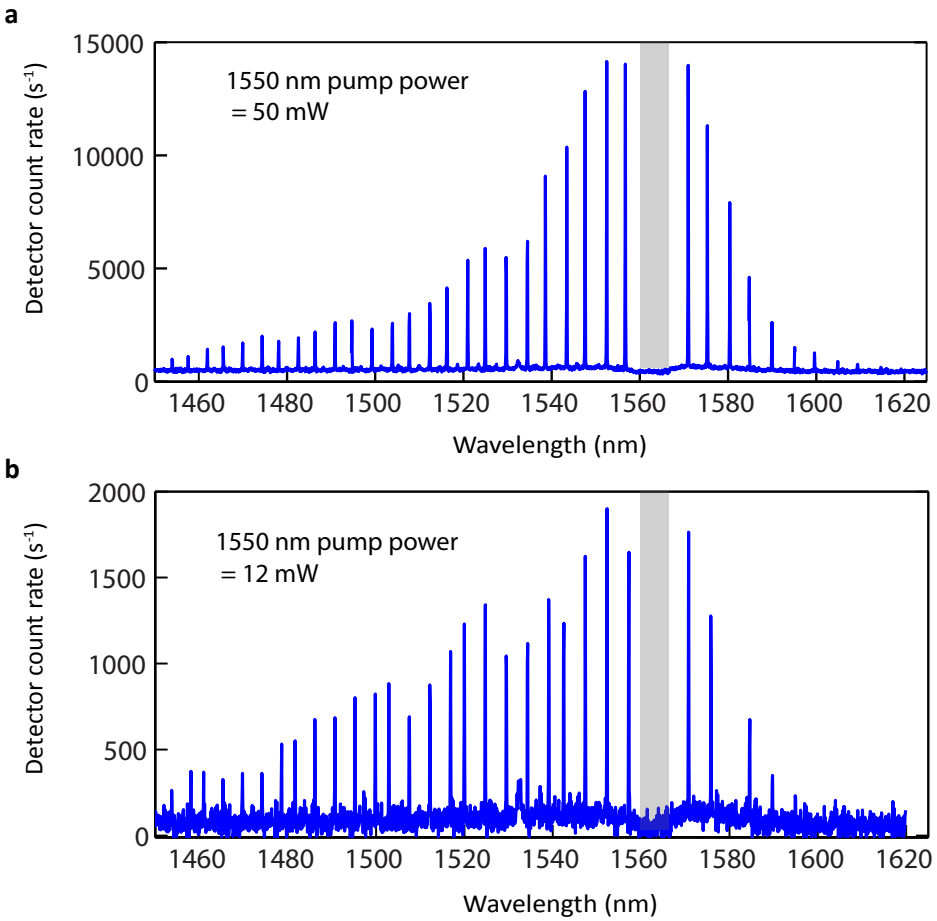

FIG. S12: **Spectrometer measurement for the noise induced by the** 1550 **nm pump when it is tuned into resonance** for **a**: pump power of 50 mW and for **b**: pump power of 12 mW. The pump is located at 1559.8 nm and has been notched out using cascaded WDMs (grey area).

noise power from such spectrometer measurements, similar to the data shown in Fig. 6c in the main paper. However, we find it is not very straightforward to calibrate the spectrometer system over such a wide spectral range, as spectra covering different wavelength spans have to be stitched together while the responses of the grating and InGaAs detector are both wavelength dependent. Moreover, because of the relatively high dark count of our system, an accurate estimation of the noise power is difficult.

Finally, we provide a brief discussion on the possible origin of the observed resonant noise in the 1550 band caused by the nearby strong pump. We notice that such noise has rarely been reported or investigated before, which could be due to (1) the noise power is small (on the order of pW) and thus is not important to many classical applications, and (2) the pump power in a conventional photoluminescence experiment may not be strong enough to observe such noise using a bulk Si_3N_4 wafer (note that for 50 mW pump power, the power circulating inside the Si_3N_4 microring is around 10 W due to resonant enhancement and the intensity is close to 2.9 GW/cm^2 because of the strong mode confinement offered by the Si_3N_4 waveguide). Possible explanations for the observed resonant noise include Raman scattering from Si_3N_4, spontaneous FWM due to high-order dispersions or mode interaction, and photoluminescence caused by material defects. We believe the first two are unlikely for the following reasons:

1. Though the Raman properties of Si_3N_4 have not been fully characterized in the literature, based on published papers[31], it seems that the Raman scattering from Si_3N_4 is not particularly strong (compared to SiO_2), and the observed Raman shift due to Si_3N_4 (in the $\approx$ 70 THz range) is too large to account for the noise measured here. Moreover, as we see from the spectra shown in Fig. S12, the noise on the anti-Stokes (higher frequency) side is stronger than the Stokes side, which is opposite of what is expected for a Raman process. In addition, we expect the spontaneous Raman noise to linearly increase with the pump power (similar to Fig. S11c), whereas the resonant noise we observed is clearly nonlinear with the pump power (Fig. 6d in the main paper).

2. The similarity of the spectra shown in Fig. S12 to a comb may lead one to consider these noise peaks to be from the spontaneous FWM, though we believe it is not the case here. First of all, the dispersion characterization (see Figs. 2e

and 2f in the main paper) shows that our microring is in the normal dispersion regime in both the 1550 nm and 980 nm bands, so there shouldn't be any parametric gain. Second, even if a spontaneous FWM process can start due to high-order dispersions or accidental mode interactions (which are absent in the 1550 nm band), such a process has very distinct power-dependant behavior: there is a threshold power below which there is no comb generation, and the comb span increases with the pump power. However, we fail to observe any threshold power level that cuts off the resonant noise (Fig. 6d in the main paper) and the noise spectrum range does not seem to depend much on the pump power (as we compare Figs. S12a and b).

For the above reasons, we tend to believe the resonant noise is more likely to be caused by the imperfect material property of Si_3N_4. In fact, the resonant noise spectral range (1460 nm to 1580 nm) is very similar to the overtone absorption band from the N-H bond in Si_3N_4[13,32]. Especially, the cutoff of the noise beyond 1600 nm despite being not far from the pump wavelength (1560 nm) clearly suggests a specific absorption window and is quite characteristic of N-H bonds. We suspect our annealing process only partially breaks these N-H bonds while the remaining ones can absorb pump photons and re-emit photons at different wavelengths. Another evidence of imperfect annealing is that the intrinsic Q of our microrings is typically higher in the 1300 nm and 980 nm bands than the 1550 nm band. At the current stage, obviously more experiments are required to identify the exact source of the noise, such as comparing the noise properties for Si_3N_4 grown under different conditions and improving the annealing process to reduce possible material defects. These tasks will be the subject of future studies. On the other hand, the results from Fig. S11b indicate a clear benefit, from a noise perspective, in inverting the pump powers in the wideband downconversion scheme so that the 980 nm power is larger than the 1550 nm power. Future studies will therefore also focus on optimizing the frequency conversion process with this scheme.

---

* Electronic address: qing.li@nist.gov
† Electronic address: kartik.srinivasan@nist.gov

[1] P. P. Absil, J. V. Hryniewicz, B. E. Little, P. S. Cho, R. A. Wilson, L. G. Joneckis, and P.-T. Ho, "Wavelength conversion in GaAs micro-ring resonators," Optics Letters **25**, 554–556 (2000).
[2] G. P. Agrawal, *Nonlinear Fiber Optics* (Academic Press, Amsterdam, 2007).
[3] M. Ferrera, L. Razzari, D. Duchesne, R. Morandotti, Z. Yang, M. Liscidini, J. E. Sipe, S. Chu, B. E. Little, and D. J. Moss, "Low-power continuous-wave nonlinear optics in doped silica glass integrated waveguide structures," Nature Photonics **2**, 737–740 (2008).
[4] M. Ferrera, D. Duchesne, L. Razzari, M. Peccianti, R. Morandotti, P. Cheben, S. Janz, D.-X. Xu, B. E. Little, S. Chu, and D. J. Moss, "Low power four wave mixing in an integrated, micro-ring resonator with Q = 1.2 million," Optics Express **17**, 14 098–14 103 (2009).
[5] A. C. Turner, M. A. Foster, A. L. Gaeta, and M. Lipson, "Ultra-low power parametric frequency conversion in a silicon microring resonator," Optics Express **16**, 4881–4887 (2008).
[6] J. R. Ong, R. Kumar, R. Aguinaldo, and S. Mookherjea, "Efficient CW Four-Wave Mixing in Silicon-on-Insulator Micro-Rings With Active Carrier Removal," IEEE Photonics Technology Letters **25**, 1699–1702 (2013).
[7] H. J. McGuinness, M. G. Raymer, C. J. McKinstrie, and S. Radic, "Quantum Frequency Translation of Single-Photon States in a Photonic Crystal Fiber," Physical Review Letters **105**, 093 604 (2010).
[8] H. McGuinness, M. Raymer, C. McKinstrie, and S. Radic, "Wavelength Translation Across 210 nm in the Visible Using Vector Bragg Scattering in a Birefringent Photonic Crystal Fiber," IEEE Photonics Technology Letters **23**, 109–111 (2011).
[9] P. S. Donvalkar, V. Venkataraman, S. Clemmen, K. Saha, and A. L. Gaeta, "Frequency translation via four-wave mixing Bragg scattering in Rb filled photonic bandgap fibers," Optics Letters **39**, 1557–1560 (2014).
[10] A. S. Clark, S. Shahnia, M. J. Collins, C. Xiong, and B. J. Eggleton, "High-efficiency frequency conversion in the single-photon regime," Optics Letters **38**, 947–949 (2013).
[11] I. Agha, M. Davanço, B. Thurston, and K. Srinivasan, "Low-noise chip-based frequency conversion by four-wave-mixing Bragg scattering in SiN x waveguides," Optics Letters **37**, 2997–2999 (2012).
[12] I. Agha, S. Ates, M. Davanço, and K. Srinivasan, "A chip-scale, telecommunications-band frequency conversion interface for quantum emitters," Optics Express **21**, 21 628–21 638 (2013).
[13] Q. Li, A. A. Eftekhar, M. Sodagar, Z. Xia, A. H. Atabaki, and A. Adibi, "Vertical integration of high-Q silicon nitride microresonators into silicon-on-insulator platform," Optics Express **21**, 18 236–18 248 (2013).
[14] A. H. Atabaki, A. A. Eftekhar, M. Askari, and A. Adibi, "Accurate post-fabrication trimming of ultra-compact resonators on silicon," Optics Express **21**, 14 139–14 145 (2013).
[15] P. Dong, W. Qian, H. Liang, R. Shafiiha, N. Feng, D. Feng, X. Zheng, A. V. Krishnamoorthy, and M. Asghari, "Low Poewr and Compact Reconfigurable Multiplexing Devices Based on Silicon Microring Resonators," Optics Express **18**, 9852–9858 (2010).
[16] E. Timurdogan, C. M. Sorace-Agaskar, J. Sun, E. S. Hosseini, A. Biberman, and M. R. Watts, "An ultralow power athermal silicon modulator," Nature Communications **5**, 4008 (2014).
[17] S. Coen, H. G. Randle, T. Sylvestre, and M. Erkintalo, "Modeling of octave-spanning Kerr frequency combs using a generalized mean-field Lugiato–Lefever model," Optics Letters **38**, 37–39 (2013).
[18] Y. K. Chembo and N. Yu, "Modal expansion approach to optical-frequency-comb generation with monolithic whispering-gallery-mode resonators," Physical Review A **82**, 033 801 (2010).

[19] T. Hansson, D. Modotto, and S. Wabnitz, "On the numerical simulation of Kerr frequency combs using coupled mode equations," Optics Communications **312**, 134–136 (2013).
[20] Y. K. Chembo and C. R. Menyuk, "Spatiotemporal Lugiato-Lefever formalism for Kerr-comb generation in whispering-gallery-mode resonators," Physical Review A **87**, 053 852 (2013).
[21] Y. Huang, V. Velev, and P. Kumar, "Quantum frequency conversion in nonlinear microcavities," Optics Letters **38**, 2119–2121 (2013).
[22] Q. Lin, T. J. Johnson, R. Perahia, C. P. Michael, and O. J. Painter, "A proposal for highly tunable optical parameteric oscillation in silicon micro-resonators," Optics Express **16**, 10 596–10 610 (2008).
[23] W. C. Jiang, X. Lu, J. Zhang, O. J. Painter, and Q. Lin, "Silicon-chip source of bright photon pairs," Optics Express **23**, 20 884–20 904 (2015).
[24] X. Zeng and M. A. Popovic, "Design of triply-resonant microphotonic parametric oscillators based on Kerr nonlinearity," Optics Express **22**, 15 837–15 867 (2014).
[25] H. A. Haus, *Waves and Fields in Optoelectronics* (Prentice-Hall, Englewood Cliffs, New Jersey, 1984), 1st edn.
[26] Q. Lin, O. J. Painter, and G. P. Agrawal, "Nonlinear optical phenomena in silicon waveguides: modeling and applications," Optics Express **15**, 16 604 (2007).
[27] E. Shah Hosseini, S. Yegnanarayanan, A. H. Atabaki, M. Soltani, and A. Adibi, "Systematic design and fabrication of high-Q single-mode pulley-coupled planar silicon nitride microdisk resonators at visible wavelengths," Optics Express **18**, 2127–2136 (2010).
[28] J. S. Levy, M. A. Foster, A. L. Gaeta, and M. Lipson, "Harmonic generation in silicon nitride ring resonators," Optics Express **19**, 11 415–11 421 (2011).
[29] Q. Lin, F. Yaman, and G. P. Agrawal, "Photon-pair generation in optical fibers through four-wave mixing: Role of Raman scattering and pump polarization," Physical Review A **75**, 023 803 (2007).
[30] R. H. Stolen, "Fundamentals of Raman Amplification in Fibers," in *Raman Amplifiers for Telecommunications 1* (Springer, 2003), chap. 2.
[31] A. Dhakal, P. Wuytens, F. Peyskens, A. Z. Subramanian, N. L. Thomas, and R. Baets, "Silicon-nitride waveguides for on-chip Raman spectroscopy," Proceedings of SPIE **9141**, 91 411C (2014).
[32] F. H. P. M. Habraken, *LPCVD Silicon Nitride and Oxynitride Films: Material and Applications in Integrated Circuit Technology* (Springer-Verlag, 1991).